Geochemistry Geophysics Geosystems G3

*Article*
Volume 12, Number 3
1 March 2011
Q03003, doi:10.1029/2010GC003397
ISSN: 1525-2027

Published by AGU and the Geochemical Society

# Analytical theory relating the depth of the sulfate-methane transition to gas hydrate distribution and saturation

**Gaurav Bhatnagar**
*Department of Chemical and Biomolecular Engineering, William Marsh Rice University, PO Box 1892, Houston, Texas 77005, USA*

*Shell Projects and Technology, Houston, Texas 77252, USA*

**Sayantan Chatterjee and Walter G. Chapman**
*Department of Chemical and Biomolecular Engineering, William Marsh Rice University, PO Box 1892, Houston, Texas 77005, USA*

**Brandon Dugan**
*Department of Earth Science, William Marsh Rice University, 6100 Main Street, MS 126, Houston, Texas 77005, USA*

**Gerald R. Dickens**
*Department of Earth Science, William Marsh Rice University, 6100 Main Street, MS 126, Houston, Texas 77005, USA*

*Institutionen för Geologiska Vetenskaper, Stockholms Universitet, SE-106 91 Stockholm, Sweden*

**George J. Hirasaki**
*Department of Chemical and Biomolecular Engineering, William Marsh Rice University, PO Box 1892, Houston, Texas 77005, USA (gjh@rice.edu)*

[1] We develop a theory that relates gas hydrate saturation in marine sediments to the depth of the sulfate-methane transition (SMT) zone below the seafloor using steady state, analytical expressions. These expressions are valid for systems in which all methane transported into the gas hydrate stability zone (GHSZ) comes from deeper external sources (i.e., advective systems). This advective constraint causes anaerobic oxidation of methane to be the only sulfate sink, allowing us to link SMT depth to net methane flux. We also develop analytical expressions that define the gas hydrate saturation profile based on SMT depth and site-specific parameters such as sedimentation rate, methane solubility, and porosity. We evaluate our analytical model at four drill sites along the Cascadia Margin where methane sources from depth dominate. With our model, we calculate average gas hydrate saturations across GHSZ and the top occurrence of gas hydrate at these sites as 0.4% and 120 mbsf (Site 889), 1.9% and 70 mbsf (Site U1325), 4.7% and 40 mbsf (Site U1326), and 0% (Site U1329), mbsf being meters below seafloor. These values compare favorably with average saturations and top occurrences computed from resistivity log and chloride data. The analytical expressions thus provide a fast and convenient method to calculate gas hydrate saturation and first-order occurrence at a given geologic setting where vertically upward advection dominates the methane flux.

**Components:** 11,600 words, 9 figures, 2 tables.

**Keywords:** gas hydrates; marine sediments; sulfate-methane transition; Cascadia Margin; analytical modeling.

**Index Terms:** 3004 Marine Geology and Geophysics: Gas and hydrate systems; 3022 Marine Geology and Geophysics: Marine sediments: processes and transport; 1009 Geochemistry: Geochemical modeling (3610, 8410).

**Received** 18 October 2010; **Revised** 7 January 2011; **Accepted** 14 January 2011; **Published** 1 March 2011.

Bhatnagar, G., S. Chatterjee, W. G. Chapman, B. Dugan, G. R. Dickens, and G. J. Hirasaki (2011), Analytical theory relating the depth of the sulfate-methane transition to gas hydrate distribution and saturation, *Geochem. Geophys. Geosyst.*, *12*, Q03003, doi:10.1029/2010GC003397.

## 1. Introduction

[2] Clathrate hydrates of gas, commonly called gas hydrates, form in the pore space of marine sediment along many continental margins [*Kvenvolden*, 1993; *Tréhu et al.*, 2006]. They are of broad scientific interest because they may represent a potential energy resource [e.g., *Collett*, 2002; *Walsh et al.*, 2009], a geohazard [e.g., *Briaud and Chaouch*, 1997; *Kwon et al.*, 2010], and a large, dynamic component of the global carbon cycle [e.g., *Dickens*, 2003; *Archer et al.*, 2009].

[3] The stability of gas hydrates depends on gas composition, temperature, pressure, and salinity. These factors collectively restrict their occurrence in marine sediment to a finite region below the seafloor, often referred to as the gas hydrate stability zone (GHSZ). Typically, however, gas hydrates only occupy a small percentage of pore space (<10%) within part of this zone because of solubility conditions and the distribution of gas with respect to depth [e.g., *Tréhu et al.*, 2006]. The amount of gas hydrate present within the GHSZ is ultimately controlled by inputs and outputs of gas over geologic timescales [*Hyndman and Davis*, 1992; *Xu and Ruppel*, 1999; *Davie and Buffett*, 2001; *Dickens*, 2003; *Hensen and Wallman*, 2005]. Inputs include in situ generation of methane by microbes and upward fluxes of gas from depth; outputs include burial, seafloor venting, and anaerobic oxidation of methane (AOM).

[4] Gas hydrate distribution and abundance in marine sediment impacts the aforementioned areas of research. Consequently, several techniques have been developed to estimate these parameters at a particular location. Most of these fall into one of two general categories: remote approaches using a moving ship, or downhole approaches involving drilling [*Tréhu et al.*, 2006]. Examples of the first include examination of seismic reflection or resistivity profiles; examples of the second include analyses of pore fluid chemical and thermal anomalies, pressurized sediment cores, or velocity and resistivity logs. In this paper, we discuss and refine a different approach: the use of pore water sulfate profiles in shallow cores.

[5] Following previous work [*Borowski et al.*, 1996, 1999; *Davie and Buffett*, 2003b; *Luff and Wallman*, 2003; *Hensen and Wallman*, 2005; *Bhatnagar et al.*, 2008; *Malinverno et al.*, 2008], we develop a one-dimensional model that relates the depth of the sulfate methane transition (SMT) to the amount and distribution of gas hydrate at depth. One advantage of this approach is that it only requires shallow piston cores. Further, it does not depend on specified baseline curves, a necessity for most other approaches used to quantify gas hydrate. Finally, it provides information concerning the top occurrence of gas hydrate within the GHSZ. Previous work has simulated gas hydrate distribution at a particular site using numerical models, and then adjusted model parameters to achieve the observed sulfate profile [*Davie and Buffett*, 2003b; *Luff and Wallman*, 2003; *Hensen and Wallman*, 2005; *Malinverno et al.*, 2008]. Our analysis differs because we develop an analytical theory for gas hydrate systems where sulfate consumption is coupled into the model. This allows gas hydrate saturation to be calculated from the sulfate profile; that is, the SMT depth, which is relatively easy to determine, becomes the primary input.

## 2. Background

### 2.1. Sulfate Depletion Above Gas Hydrate

[6] Seafloor settings where gas hydrate has been recovered, or is inferred to exist, invariably have a sulfate-methane transition (SMT) at a relatively shallow depth (0–30 m) below the seafloor [e.g., *Borowski et al.*, 1999; *Tréhu et al.*, 2004; *Riedel et al.*, 2006; *Snyder et al.*, 2007]. This usually thin (<2 m) sediment horizon is characterized by near depletion of pore water $CH_4$ and $SO_4^{2-}$ concentrations (Figure 1). Above, dissolved sulfate concentrations increase toward seawater concentrations at or near the seafloor (and there is negligible methane); below, dissolved methane concentrations increase

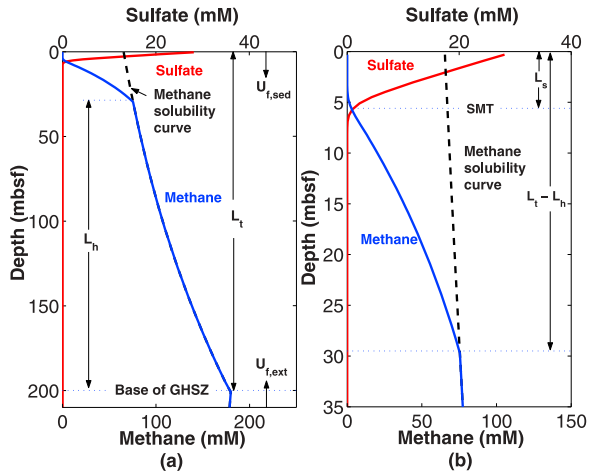


**Figure 1.** (a) Schematic representation of a gas hydrate system showing pore water sulfate and methane concentrations, which go to zero at some shallow depth because of anaerobic oxidation of methane (AOM). Also shown are methane solubility in water, the two fluid fluxes ($U_{f,sed}$ and $U_{f,ext}$), and depth to the base of the gas hydrate stability zone ($L_t$). (b) Close-up of the sulfate-methane transition (SMT) showing overlap of sulfate and methane profiles, its depth below the seafloor ($L_s$), and the depth to the top of the gas hydrate layer ($L_h$).

toward the shallowest occurrence of gas hydrate (and there is negligible sulfate). We prefer the phrase SMT to sulfate-methane interface (SMI) because sampling and analyses at high spatial resolution typically show that methane and sulfate profiles intersect at nonzero concentrations, making this a sediment interval with measurable thickness.

[7] Two microbially mediated reactions remove dissolved sulfate from pore waters of marine sediment. In the absence of methane, reaction with solid organic (organoclastic reduction) can occur [e.g., *Berner*, 1980; *Boudreau and Westrich*, 1984]. Sulfate consumption can also proceed by anaerobic oxidation of methane (AOM) [e.g., *Valentine and Reeburgh*, 2000]:

$$CH_4 + SO_4^{2-} \rightarrow HCO_3^- + HS^- + H_2O. \quad (1)$$

Both reactions could, singly or collectively, cause an SMT in marine sediment sequences that host gas hydrates [cf. *Kastner et al.*, 2008; *Dickens and Snyder*, 2009]. Organoclastic reduction can remove sulfate in uppermost sediment, after which microbes use remaining solid organic carbon to produce methane [*Martens and Berner*, 1974]. Alternatively, methane produced at depth, including by microbes [*Yoshioka et al.*, 2010], can move up by diffusion, advection, or both, and drive AOM at the SMT. The presence of gas hydrates beneath the seafloor implies a high upward flux of methane, even in regions with minimal fluid advection [e.g., *Borowski et al.*, 1999; *Davie and Buffett*, 2003b; *Dickens and Snyder*, 2009]. This fact necessitates a major role for the second process in these locations.

[8] SMT depths in regions with gas hydrate almost assuredly relate to the flux of methane rising from deeper sediment. This is obvious within small regions of the seafloor where sediment cores have been retrieved and examined across locations of active methane venting. In these cases, the supply of solid organic carbon to the seafloor is similar, but the SMT systematically shoals toward the sediment-water interface around locations of elevated methane flux [e.g., *Paull et al.*, 2005; *Castellini et al.*, 2006; *Pape et al.*, 2010]. Somewhat analogous observations have been made across broader regions of the seafloor. For example, a general link occurs between seismic indications for gas hydrate and the depth of the SMT on Blake Ridge [*Borowski et al.*, 1996, 1999].

[9] The simplest explanation is that AOM within the SMT dominates *net* consumption of dissolved sulfate in shallow sediment of regions with gas hydrate, especially where advection brings a high methane flux toward the seafloor [*Borowski et al.*, 1996, 1999]. This inference is supported, in many cases, by two observations. First, sulfate concentrations often drop near-linearly above the SMT (at least where advection of sulfate-free water is not too high). This suggests minimal *net* sulfate consumption between the seafloor and the SMT, and substantial sulfate consumption at the SMT [*Borowski et al.*, 1996, 1999; *Dickens*, 2001; *Davie and Buffett*, 2003b; *Snyder et al.*, 2007; *Bhatnagar et al.*, 2008]. Second, dissolved constituents released during reduction of solid organic (e.g., N species) do not show excess generation across the SMT [*Borowski et al.*, 1996, 1999]. Very few studies have tried to account for all carbon *fluxes* in shallow sediment above gas hydrate systems, especially including dissolved bicarbonate rising from deeper sediment. However, these indicate that AOM at the SMT consumes most of the *net* dissolved sulfate in shallow sediment of regions with gas hydrate [*Luff and Wallman*, 2003; *Snyder et al.*, 2007; *Dickens and Snyder*, 2009].

[10] Realization that AOM dominates *net* sulfate consumption in shallow sediment of regions con-

taining gas hydrate has an important implication. At steady state conditions, there should be a 1:1 relationship between the downward flux of sulfate and the upward flux of methane, and the depth of the SMT should relate to both [e.g., *Borowski et al.*, 1996; *Dickens and Snyder*, 2009].

## 2.2. Modeling

[11] The upward methane flux into shallow sediment depends on the net fluid flux as well as the methane concentration of the rising pore water. Results of previous modeling suggest that, at steady state conditions, gas hydrate extends to the base of the GHSZ if methane supplied from depth exceeds some critical value [*Xu and Ruppel*, 1999; *Bhatnagar et al.*, 2007]. This is probably the case for many locations with gas hydrate because sedimentation brings solid gas hydrate to the base of the GHSZ [e.g., *Bhatnagar et al.*, 2007]. The widespread presence of bottom simulating reflectors (BSRs), which indicate gas hydrate and free gas at the base of the GHSZ [*Kvenvolden*, 1993, *Holbrook et al.*, 1996; *Tréhu et al.*, 2006], supports this concept from a field perspective.

[12] Several modeling studies have argued that net upward fluid flux affects pore water methane and sulfate concentration profiles [*Davie and Buffett*, 2003b; *Bhatnagar et al.*, 2008; *Malinverno et al.*, 2008], and thus the depth to the SMT, as well as the average gas hydrate flux through the GHSZ [*Bhatnagar et al.*, 2008]. The model developed by *Bhatnagar et al.* [2008] led to a generalized plot between the scaled SMT depth ($\tilde{L}_s$) and the average gas hydrate flux ($Pe_1\langle S_h\rangle$). Several different parameter sets generalized this relationship, but the simulation methodology suffered from a few disadvantages. First, the generalized plot between scaled SMT depth and gas hydrate flux, which represents the downward burial of gas hydrate, only yielded the average gas hydrate saturation within the GHSZ [*Bhatnagar et al.*, 2008]. To obtain the gas hydrate saturation profile with depth, new simulations had to be performed. Second, the relation between gas hydrate flux and SMT depth was generalized for certain parameter values (for example, constant porosity behavior, seafloor temperature and depth, geothermal gradient) [*Bhatnagar et al.*, 2008]. By deriving analytical expressions, exact solutions for the concentration profiles, hydrate saturation profile and thickness of the hydrate layer can be obtained for site-specific parameters without performing complex numerical simulations. Thus our new, analytical approach is applicable to any system where the methane flux exceeds some critical value.

# 3. Mathematical Model

## 3.1. Overview

[13] We derive a relationship between the depth of the SMT and the upward methane flux using a steady state mass balance equation for sulfate. This enables calculation of the sulfate concentration profile as a function of depth below the seafloor. We then use the equality of sulfate and methane molar fluxes at the SMT to express results in terms of methane flux. This is followed by developing a two-phase, steady state methane balance for the system, which links gas hydrate occurrence and gas hydrate saturation to methane flux. Finally, by "eliminating" methane flux between sulfate and methane mass balances, we show how the SMT depth relates to the thickness and amount of gas hydrate. All equations are converted to dimensionless form to reduce the number of free parameters. However, we show how these dimensionless equations translate to dimensional field data.

## 3.2. Sulfate Mass Balance

[14] Two assumptions underpin the sulfate mass balance: (1) no *net* sulfate depletion occurs above the SMT due to organoclastic reduction, and (2) dissolved methane and sulfate react (by AOM) at the SMT fast enough such that their concentrations drop to zero at a single depth. The presence of a "transition," where methane and sulfate coexist across a depth zone, albeit thin, suggests AOM occurs within a finite volume instead of at a sharp interface. However, when sediment depths are normalized to the depth to the base of the GHSZ, the relative thickness of the SMT approaches a sharp interface.

[15] The steady state sulfate mass balance is

$$\frac{d}{dz}\left[U_f\rho_w c_s^l - \phi\rho_w D_s\frac{dc_s^l}{dz}\right] = 0,\ \ 0 < z < L_s, \qquad (2)$$

where $U_f$ is the net fluid flux, $\rho_w$ is pore water density, $c_s^l$ is the mass fraction of sulfate in pore water, $\phi$ is porosity, $D_s$ is sulfate diffusivity, $L_s$ is the depth to the SMT, and $z$ is the depth below seafloor (positive downward) (Figure 1). This mass balance implies that the mass flux of sulfate, $F_{SO_4}$, remains constant above the SMT, and can be rewritten as

$$U_f\rho_w c_s^l - \phi\rho_w D_s\frac{dc_s^l}{dz} = F_{SO_4},\ \ 0 < z < L_s. \qquad (3)$$

To recast this relation in dimensionless form, the vertical depth is normalized by $L_t$, the depth to the base of the GHSZ ($\tilde{z} = z/L_t$; $\tilde{L}_s = L_s/L_t$), while sulfate concentration is scaled by $c_{s,o}$, its value in standard seawater ($\tilde{c}_s^l = c_s^l/c_{s,o}$).

[16] The net fluid flux ($U_f$) can be written as the sum of two components: $U_{f,sed}$ due to sedimentation and compaction; and $U_{f,ext}$ due to upward external flow (section A1). This enables definition of two Peclet numbers that compare each part of the fluid flux to methane diffusion:

$$Pe_1 = \frac{U_{f,sed}L_t}{D_m},\ Pe_2 = \frac{U_{f,ext}L_t}{D_m}, \tag{4}$$

where $D_m$ denotes diffusivity of methane. In turn, $U_{f,sed}$, and hence $Pe_1$, can be related to the sedimentation rate at the seafloor ($\dot{S}$) and porosity parameters using steady state burial models [*Berner*, 1980; *Davie and Buffett*, 2003b; *Bhatnagar et al.*, 2007] (section A1).

[17] The dimensionless sulfate balance is

$$\left(\frac{1+\gamma}{\gamma}\right)(Pe_1+Pe_2)\tilde{c}_s^l - \left(\frac{1+\gamma\tilde{\phi}}{\gamma}\right)\frac{D_s}{D_m}\frac{d\tilde{c}_s^l}{d\tilde{z}} = \left(\frac{1}{1-\phi_\infty}\right)\frac{F_{SO_4}}{\rho_w c_{s,o}}\frac{L_t}{D_m}, 0 < \tilde{z} < \tilde{L}_s, \tag{5}$$

where $\tilde{\phi}$ is the reduced porosity $\left(=\frac{\phi-\phi_\infty}{1-\phi_\infty}\right)$, $\gamma$ is $\left(\frac{1-\phi_\infty}{\phi_\infty}\right)$, and $\phi_\infty$ is the minimum porosity achieved at great depth. The porosity model assumes hydrostatic pore pressure and equilibrium compaction, and the details of nondimensionalization are given later (section A1). To simplify the notation, however, we define the following groups:

$$\left(\frac{1+\gamma}{\gamma}\right)(Pe_1+Pe_2) = Q, \text{ and} \tag{6}$$

$$\left(\frac{1}{1-\phi_\infty}\right)\frac{F_{SO_4}}{\rho_w c_{s,o}}\frac{L_t}{D_m} = f_{SO_4}, \tag{7}$$

where $Q$ denotes the dimensionless net fluid flux and $f_{SO_4}$ is a dimensionless sulfate flux. Using these definitions, equation (5) becomes

$$Q\tilde{c}_s^l - \left(\frac{1+\gamma\tilde{\phi}}{\gamma}\right)\tilde{D}_s\frac{d\tilde{c}_s^l}{d\tilde{z}} = f_{SO_4}, \tag{8}$$

where $\tilde{D}_s$ is the ratio of sulfate to methane diffusivity.

[18] Two boundary conditions (B.C.) enable an analytical relationship between downward sulfate flux and SMT depth. The first is applied at the seafloor, where normalized sulfate concentration equals unity; the second is applied at the SMT, where normalized sulfate concentration is zero:

$$\text{B.C.}: \tilde{c}_s^l = 1 \text{ at } \tilde{z} = 0, \text{ and} \tag{9}$$

$$\text{B.C.}: \tilde{c}_s^l = 0 \text{ at } \tilde{z} = \tilde{L}_s. \tag{10}$$

With these B.C.s, equation (8) can be rearranged to:

$$\int_{\tilde{L}_s}^{0}\left(\frac{\gamma}{1+\gamma\tilde{\phi}}\right)d\tilde{z} = \int_0^1\left(\frac{\tilde{D}_s}{Q\tilde{c}_s^l - f_{SO_4}}\right)d\tilde{c}_s^l. \tag{11}$$

Integrating equation (11) yields

$$g(\tilde{z})\Big|_{\tilde{z}=0} - g(\tilde{z})\Big|_{\tilde{z}=\tilde{L}_s} = \frac{\tilde{D}_s}{Q}\ln\left(1-\frac{Q}{f_{SO_4}}\right),\ 0 < \tilde{z} < \tilde{L}_s, \tag{12}$$

where $g(\tilde{z})$ represents the integral of the porosity term on the left hand side of equation (11), or

$$g(\tilde{z}) = \frac{\gamma N_{t\phi}\tilde{z} + \gamma^2\ln(\eta(1+\gamma)+(1-\eta)e^{N_{t\phi}\tilde{z}})}{(1+\gamma)N_{t\phi}}. \tag{13}$$

Rearranging equation (12), and denoting the function evaluations by $g(0)$ and $g(\tilde{L}_s)$, the following describes the relation between sulfate flux and SMT depth:

$$f_{SO_4} = \frac{Q}{1-\exp\left(\frac{Q}{\tilde{D}_s}\left[g(0)-g(\tilde{L}_s)\right]\right)}. \tag{14}$$

[19] To obtain the steady state sulfate concentration profile, equation (8) is integrated from any depth ($\tilde{z}$) to scaled SMT depth ($\tilde{L}_s$), which yields

$$g(\tilde{z}) - g(\tilde{L}_s) = \frac{\tilde{D}_s}{Q}\ln\left(1-\frac{Q\tilde{c}_s^l(\tilde{z})}{f_{SO_4}}\right),\ 0 < \tilde{z} < \tilde{L}_s. \tag{15}$$

Rearranging this equation renders

$$\frac{Q\tilde{c}_s^l(\tilde{z})}{f_{SO_4}} = 1-\exp\left(\frac{Q}{\tilde{D}_s}\left[g(\tilde{z})-g(\tilde{L}_s)\right]\right),\ 0 < \tilde{z} < \tilde{L}_s. \tag{16}$$

Finally, substituting the expression for $f_{SO_4}$ (equation (14)) into equation (16) gives the sulfate concentration profile at steady state:

$$\tilde{c}_s^l(\tilde{z}) = \frac{1 - \exp\left(\frac{Q}{\tilde{D}_s}\left[g(\tilde{z}) - g(\tilde{L}_s)\right]\right)}{1 - \exp\left(\frac{Q}{\tilde{D}_s}\left[g(0) - g(\tilde{L}_s)\right]\right)}, \; 0 < \tilde{z} < \tilde{L}_s. \quad (17)$$

This steady state sulfate concentration profile is a function of the scaled SMT depth, $\tilde{L}_s$, scaled diffusivity, $\tilde{D}_s$, and the net fluid flux, $Q$.

## 3.3. Relationship Between Sulfate and Methane Fluxes

[20] At the SMT, the molar fluxes of methane and sulfate should equal due to the 1:1 stoichiometry of the AOM reaction (equation (1)). Thus, the downward sulfate mass flux ($f_{SO_4}$) can be written in terms of the upward methane mass flux ($F_{CH_4}$):

$$F_{SO_4} = -\frac{M_{SO_4}}{M_{CH_4}} F_{CH_4}, \;\; \text{at} \;\; \tilde{z} = \tilde{L}_s, \quad (18)$$

where $M_i$ denotes molecular weight (and the negative sign arises from the difference in direction). Substituting equation (18) into equation (7) yields

$$f_{SO_4} = -\left(\frac{1}{1 - \phi_\infty}\right) \frac{1}{\rho_w c_{s,o}} \frac{L_t}{D_m} \frac{M_{SO_4}}{M_{CH_4}} F_{CH_4}. \quad (19)$$

To simplify the notation, we introduce a dimensionless methane flux $f_{CH_4}$:

$$f_{CH_4} = \left(\frac{1}{1 - \phi_\infty}\right) \frac{1}{\rho_w c^l_{m,eqb}} \frac{L_t}{D_m} F_{CH_4}, \quad (20)$$

where $c^l_{m,eqb}$ is the methane solubility at the base of GHSZ. Using this notation, equation (19) can be used to express the dimensionless methane flux in terms of the dimensionless sulfate flux:

$$f_{CH_4} = -f_{SO_4}/m, \;\; \text{where} \;\; m = \frac{M_{SO_4}}{M_{CH_4}} \frac{c^l_{m,eqb}}{c_{s,o}}. \quad (21)$$

Thus, we can obtain an expression between the scaled SMT depth ($\tilde{L}_s$) and methane flux ($f_{CH_4}$):

$$f_{CH_4} = -f_{SO_4}/m = \frac{-Q/m}{1 - \exp\left(\frac{Q}{\tilde{D}_s}\left[g(0) - g(\tilde{L}_s)\right]\right)}. \quad (22)$$

## 3.4. Methane Mass Balance

[21] Analogous mass balance equations can be derived for methane (and water) over two spatial domains. The first domain extends from the SMT to the top of gas hydrate, whereas the second domain extends from the top of gas hydrate to the base of the GHSZ (Figure 1). These two mass balances, coupled with the sulfate balance, ultimately can be used to solve for the thickness of the gas hydrate layer and the net fluid flux using SMT depth as an input.

[22] Across both domains (i.e., from the SMT to the base of the GHSZ), the two-phase (aqueous and hydrate), steady state, methane mass balance is

$$\frac{d}{dz}\left[U_f \rho_w c^l_m + \frac{U_s}{1 - \phi} \phi S_h c^h_m \rho_h - \phi(1 - S_h)\rho_w D_m \frac{dc^l_m}{dz}\right] = 0, \; L_s < z < L_t, \quad (23)$$

where $U_s$ denotes sediment flux, $S_h$ denotes gas hydrate saturation (volume fraction of pore space), and $c^h_m$ denotes the methane mass fraction in the hydrate phase (a constant, $c^h_m = 0.134$ for structure I hydrate [*Sloan and Koh*, 2007]). The three terms in equation (23) correspond to advection of dissolved methane in pore water, advection of methane with the hydrate phase, and diffusion of methane in pore water. This methane flux invariance can be restated as

$$U_f \rho_w c^l_m + \frac{U_s}{1 - \phi} \phi S_h c^h_m \rho_h - \phi(1 - S_h)\rho_w D_m \frac{dc^l_m}{dz} = F_{CH_4}, \; L_s < z < L_t. \quad (24)$$

To nondimensionalize this equation, we scale sediment flux by $U_{f,sed}$, the two methane mass fractions by methane solubility at the base of the GHSZ ($c^l_{m,eqb}$) and gas hydrate density by the pore water density as follows:

$$\tilde{U}_s = \frac{U_s}{U_{f,sed}}, \; \tilde{c}^l_m = \frac{c^l_m}{c^l_{m,eqb}}, \; \tilde{c}^h_m = \frac{c^h_m}{c^l_{m,eqb}}, \; \tilde{\rho}_h = \frac{\rho_h}{\rho_w}. \quad (25)$$

$U_s$ and $\tilde{U}_s$ can be related to sedimentation rate and porosity parameters (section A1). Using the water mass balance, the methane mass balance (equation (24)) is rewritten in the following dimensionless form (section A2):

$$Q\tilde{c}^l_m + \frac{Pe_1 \tilde{U}_s}{1 - \tilde{\phi}}\left(\frac{1 + \gamma}{\gamma}\right)\left(\frac{1 + \gamma\tilde{\phi}}{\gamma}\right) S_h \tilde{\rho}_h \left(\tilde{c}^h_m - c^h_w \tilde{c}^l_m\right) - \left(\frac{1 + \gamma\tilde{\phi}}{\gamma}\right)(1 - S_h)\frac{d\tilde{c}^l_m}{d\tilde{z}} = f_{CH_4}, \; \tilde{L}_s < \tilde{z} < 1. \quad (26)$$

### 3.4.1. Domain 1: Interval With Only Dissolved Methane [$\tilde{L}_s < \tilde{z} < 1 - \tilde{L}_h$]

[23] We define the interval between the top occurrence of gas hydrate and the base of the GHSZ as $L_h$ which makes the depth from the seafloor to the first gas hydrate $L_t - L_h$ (Figure 1). In normalized form, the thickness of sediment with gas hydrate is $\tilde{L}_h = L_h/L_t$, while the depth to the top of gas hydrate is $(1 - \tilde{L}_h)$. For Domain 1 ($\tilde{L}_s < \tilde{z} < 1 - \tilde{L}_h$), no gas hydrate exists, and equation (26) can be simplified by setting $S_h = 0$:

$$Q\tilde{c}_m^l - \left(\frac{1+\gamma\tilde{\phi}}{\gamma}\right)\frac{d\tilde{c}_m^l}{d\tilde{z}} = f_{CH_4},\ \tilde{L}_s < \tilde{z} < 1 - \tilde{L}_h. \quad (27)$$

Methane concentration varies across this depth interval such that it is zero at the base of the SMT ($\tilde{L}_s$), and equal to that predicted by the solubility curve at the top of gas hydrate. Hence, the two boundary conditions for this equation are

$$\text{B.C.}(1) : \tilde{c}_m^l = 0,\ \text{at}\ \tilde{z} = \tilde{L}_s \quad (28)$$

$$\text{B.C.}(2) : \tilde{c}_m^l = \tilde{c}_{m,sol}\Big|_{(1-\tilde{L}_h)},\ \text{at}\ \tilde{z} = 1 - \tilde{L}_h, \quad (29)$$

where $\tilde{c}_{m,sol}(\tilde{z})$ is the normalized methane solubility curve within the GHSZ. This normalized solubility curve is obtained by scaling the methane solubility in pore water ($c_{m,sol}(\tilde{z})$) by the equilibrium solubility at the base of the GHSZ ($c^l_{m,eqb}$). This scaling yields

$$\tilde{c}_{m,sol}(\tilde{z}) = c_{m,sol}(\tilde{z})/c^l_{m,eqb}. \quad (30)$$

Equation (27) can be integrated with the above boundary conditions:

$$\int_{\tilde{L}_s}^{1-\tilde{L}_h}\left(\frac{\gamma}{1+\gamma\tilde{\phi}}\right)d\tilde{z} = \int_0^{\tilde{c}_{m,sol}\big|_{1-\tilde{L}_h}}\left(\frac{1}{Q\tilde{c}_m^l - f_{CH_4}}\right)d\tilde{c}_m^l. \quad (31)$$

Using the function $g(\tilde{z})$ (equation (13)), equation (31) becomes

$$g(1-\tilde{L}_h) - g(\tilde{L}_s) = \frac{1}{Q}\ln\left(1 - \frac{Q\tilde{c}_{m,sol}\big|_{1-\tilde{L}_h}}{f_{CH_4}}\right), \quad (32)$$

which can be rearranged to yield the methane flux in terms of the two scaled depths ($\tilde{L}_s$ and $\tilde{L}_h$):

$$f_{CH_4} = \frac{Q\tilde{c}_{m,sol}\big|_{(1-\tilde{L}_h)}}{1 - \exp\left(Q\left[g(1-\tilde{L}_h) - g(\tilde{L}_s)\right]\right)}. \quad (33)$$

[24] The methane concentration profile in this region is obtained in a manner similar to the sulfate concentration profile (section 3.2). The steady state methane concentration profile is

$$\tilde{c}_m^l(\tilde{z}) = \tilde{c}_{m,sol}\Big|_{(1-\tilde{L}_h)}\frac{1 - \exp\left(Q\left[g(\tilde{z}) - g(\tilde{L}_s)\right]\right)}{1 - \exp\left(Q\left[g(1-\tilde{L}_h) - g(\tilde{L}_s)\right]\right)},\quad \tilde{L}_s < \tilde{z} < 1 - \tilde{L}_h. \quad (34)$$

### 3.4.2. Domain 2: Interval With Gas Hydrate [$1 - \tilde{L}_h < \tilde{z} < 1$]

[25] In this sediment interval, pore water methane concentration is constrained by the methane solubility curve, which was defined as $\tilde{c}_{m,sol}(\tilde{z})$. Thus, instead of pore water methane concentration being the primary unknown, gas hydrate saturation ($S_h$) becomes the primary dependent variable. Substituting $\tilde{c}_{m,sol}(\tilde{z})$ for the pore water concentration $\tilde{c}^l_m(\tilde{z})$ into equation (26), we get the following expression:

$$Q\tilde{c}_{m,sol}(\tilde{z}) + \frac{Pe_1\tilde{U}_s}{1-\tilde{\phi}}\left(\frac{1+\gamma}{\gamma}\right)\left(\frac{1+\gamma\tilde{\phi}}{\gamma}\right)S_h\tilde{\rho}_h\left(\tilde{c}^h_m - c^h_w\tilde{c}_{m,sol}(\tilde{z})\right) - \left(\frac{1+\gamma\tilde{\phi}}{\gamma}\right)(1-S_h)\tilde{c}'_{m,sol}(\tilde{z}) = f_{CH_4}, 1 - \tilde{L}_h < \tilde{z} < 1, \quad (35)$$

where $\tilde{c}'_{m,sol}(\tilde{z})$ denotes the derivative of the solubility curve at any given depth $\tilde{z}$.

[26] The distribution of gas hydrate between the top occurrence of gas hydrate and the base of the GHSZ is complex at the m scale because of changes in lithology and other factors [e.g., *Egeberg and Dickens*, 1999; *Tréhu et al.*, 2004; *Riedel et al.*, 2006; *Malinverno et al.*, 2008]. Nonetheless, at multiple locations, there appears to be a first-order increase with depth toward the base of the GHSZ [e.g., *Westbrook et al.*, 1994; *Egeberg and Dickens*, 1999; *Tréhu et al.*, 2004]. More crucially, there should be an incremental increase in gas hydrate abundance near the top occurrence of gas hydrate, so that minimal amounts exist where total methane concentrations in pore space equal methane concentrations on the methane solubility curve (Figure 1). If this were not the case, there would be marked changes in physical properties and geophysical signatures in sediment between the seafloor and the base of the GHSZ, rather than gradual ones. Following others [*Davie and Buffett*, 2001, 2003a; *Bhatnagar et al.*, 2007, 2008], this concept im-

poses a basic constraint: gas hydrate saturation goes to zero as depths approach the top occurrence of gas hydrate layer from below. This condition can be written as

$$S_h \to 0, \text{ as } \tilde{z} \to \left(1-\tilde{L}_h\right)^+. \tag{36}$$

Substituting this condition into equation (35) gives

$$Q\tilde{c}_{m,sol}(\tilde{z}) - \left(\frac{1+\gamma\tilde{\phi}}{\gamma}\right)\tilde{c}'_{m,sol}(\tilde{z}) = f_{CH_4}, \text{ as } \tilde{z} \to \left(1-\tilde{L}_h\right)^+. \tag{37}$$

[27] There are now three equations (22), (33), and (37) in terms of four unknowns ($\tilde{L}_s$, $f_{CH_4}$, $Q$, and $\tilde{L}_h$). By using the scaled SMT depth ($\tilde{L}_s$) as an input from site data, the other three unknowns can be calculated.

## 3.5. Coupled Equations for Normalized Depths ($L_s$ and $L_h$)

[28] Two nonlinear, coupled equations can be derived in terms of three variables, $\tilde{L}_s$, $\tilde{L}_h$ and $Q$. This is achieved by rearranging the three mass balance equations (22), (33), and (37) so as to remove $f_{CH_4}$. First, $f_{CH_4}$ is "eliminated" from equations (22) and (33), by equating the downward sulfate flux to the upward methane flux at the SMT:

$$\frac{-Q/m}{1-\exp\left(\frac{Q}{\tilde{D}_s}\left[g(0)-g\left(\tilde{L}_s\right)\right]\right)} = \frac{Q\tilde{c}_{m,sol}\Big|_{\left(1-\tilde{L}_h\right)}}{1-\exp\left(Q\left[g\left(1-\tilde{L}_h\right)-g\left(\tilde{L}_s\right)\right]\right)}. \tag{38}$$

Second, $f_{CH_4}$ is "eliminated" from equations (33) and (37) be equating the methane flux in the region containing only dissolved methane to that in the region containing dissolved methane and gas hydrate:

$$\frac{Q\tilde{c}_{m,sol}\Big|_{\left(1-\tilde{L}_h\right)}}{1-\exp\left(Q\left[g\left(1-\tilde{L}_h\right)-g\left(\tilde{L}_s\right)\right]\right)} = Q\tilde{c}_{m,sol}\Big|_{\left(1-\tilde{L}_h\right)} - \left(\frac{1+\gamma\tilde{\phi}}{\gamma}\right)\tilde{c}'_{m,sol}\Big|_{\left(1-\tilde{L}_h\right)}. \tag{39}$$

[29] Once $\tilde{L}_s$ is known for a particular site, equations (38) and (39) can be solved iteratively (e.g., using a Newton-Raphson or bisection algorithm) to get the scaled thickness $\tilde{L}_h$ and sum of Peclet numbers ($Q$). Apart from $\tilde{L}_s$, the site-specific parameters needed to completely specify the system include the minimum and maximum reduced porosities ($\gamma$ and $\eta$ (section A1)), the ratio of depth to the base of the GHSZ to the compaction depth ($N_{t\phi}$), the diffusivity ratio ($\tilde{D}_s$), parameter $m$ (equation (21)), and the methane solubility curve within the GHSZ ($\tilde{c}_{m,sol}(\tilde{z})$). It should be noted that the Peclet numbers occur in equations (38) and (39) as the sum, $Q$, rather than $Pe_1$ or $Pe_2$. This implies that separate values are not needed to calculate the steady state concentration profiles or $\tilde{L}_h$. However, $Pe_1$ needs to be specified to compute the gas hydrate saturation profile, because this depends on sedimentation rate [*Davie and Buffett*, 2001; *Bhatnagar et al.*, 2007, 2008].

## 3.6. Gas Hydrate Saturation Profile

[30] A major advantage of the above formulation is that, beyond linking the depth of the SMT to the top occurrence of gas hydrate ($1-\tilde{L}_h$), it gives an analytical expression for the amount of gas hydrate, assuming steady state conditions. Following from equation (35), the gas hydrate saturation profile below the top of the hydrate layer can be rewritten as

$$\frac{Pe_1\tilde{U}_s}{1-\tilde{\phi}}\left(\frac{1+\gamma}{\gamma}\right)\left(\frac{1+\gamma\tilde{\phi}}{\gamma}\right)S_h\tilde{\rho}_h\left(\tilde{c}^h_m - c^h_w\tilde{c}_{m,sol}(\tilde{z})\right) - \left(\frac{1+\gamma\tilde{\phi}}{\gamma}\right)(1-S_h)\tilde{c}'_{m,sol}(\tilde{z}) = f_{CH_4} - Q\tilde{c}_{m,sol}(\tilde{z}), \quad 1-\tilde{L}_h < \tilde{z} < 1. \tag{40}$$

Upon rearranging, the gas hydrate saturation can be expressed as a function of scaled depth $\tilde{z}$:

$$S_h(\tilde{z}) = \frac{\left(\frac{f_{CH_4} - Q\tilde{c}_{m,sol}(\tilde{z})}{\left(\frac{1+\gamma\tilde{\phi}}{\gamma}\right)}\right) + \tilde{c}'_{m,sol}(\tilde{z})}{\left[\frac{Pe_1\tilde{U}_s}{1-\tilde{\phi}}\frac{1+\gamma}{\gamma}\tilde{\rho}_h\left(\tilde{c}^h_m - c^h_w\tilde{c}_{m,sol}(\tilde{z})\right) + \tilde{c}'_{m,sol}(\tilde{z})\right]}, \quad 1-\tilde{L}_h < \tilde{z} < 1. \tag{41}$$

[31] As mentioned in section 3.5, specifying the normalized SMT depth ($\tilde{L}_s$) allows calculation of $\tilde{L}_h$ and $Q$ through solution of the coupled equations (38) and (39). Substituting these variables into any of the methane flux expressions (e.g., equation (33)) yields the methane flux $f_{CH_4}$. Using these values and other system parameters,

equation (41) gives the steady state gas hydrate saturation profile within the GHSZ.

[32] The hydrate saturation profile, as given in equation (41), cannot exceed unity at any depth. This constraint manifests as a minimum value of $Pe_1$, below which the analytical steady state solution is not valid; i.e., values of $Pe_1$ less than this minimum yield hydrate saturations higher than unity. Equation (41) can be written such that the numerator is always less than or equal to the denominator, as follows:

$$\left(\frac{f_{CH_4}-Q\tilde{c}_{m,sol}(\tilde{z})}{\left(\frac{1+\gamma\tilde{\phi}}{\gamma}\right)}\right)+\tilde{c}'_{m,sol}(\tilde{z}) \le \left[\frac{Pe_1\tilde{U}_s}{1-\tilde{\phi}}\frac{1+\gamma}{\gamma}\tilde{\rho}_h\left(\tilde{c}^h_m-c^h_w\tilde{c}_{m,sol}(\tilde{z})\right)+\tilde{c}'_{m,sol}(\tilde{z})\right]. \quad (42)$$

Rearranging equation (42), we obtain

$$Pe_1 \ge \frac{\left(\frac{f_{CH_4}-Q\tilde{c}_{m,sol}(\tilde{z})}{\left(\frac{1+\gamma\tilde{\phi}}{\gamma}\right)}\right)}{\left[\frac{\tilde{U}_s}{1-\tilde{\phi}}\frac{1+\gamma}{\gamma}\tilde{\rho}_h\left(\tilde{c}^h_m-c^h_w\tilde{c}_{m,sol}(\tilde{z})\right)\right]}. \quad (43)$$

Steady state modeling has shown that hydrate saturation $S_h$ is maximum at $\tilde{z} = 1$. Hence, the above inequality can be written as

$$Pe_1 \ge \frac{f_{CH_4}-Q}{\left[\frac{\tilde{U}_s}{1-\tilde{\phi}}\frac{1+\gamma}{\gamma}\tilde{\rho}_h\left(\tilde{c}^h_m-c^h_w\right)\right]\left(\frac{1+\gamma\tilde{\phi}}{\gamma}\right)}, \quad \text{since } \tilde{c}_{m,sol}|_{\tilde{z}=1}=1. \quad (44)$$

Equation (44) provides the minimum value of $Pe_1$ for which our model is valid. This minimum $Pe_1$ corresponds to a minimum sedimentation rate that can be used as an input to our model. Sedimentation rate (or $Pe_1$) lower than this minimum will lead to complete clogging of the pore space, at which point our model assumptions do not hold.

## 3.7. Relating Gas Hydrate Flux to Scaled SMT Depth

[33] We have shown through numerical simulations that the steady state gas hydrate flux through the GHSZ is related to the scaled SMT depth, through their dependence on the net fluid flux in the system [*Bhatnagar et al.*, 2008]. The average gas hydrate flux was defined as the product of the Peclet number, $Pe_1$, and gas hydrate saturation averaged over the entire GHSZ, $\langle S_h\rangle$. This relationship helps in the estimation of $\langle S_h\rangle$ from $\tilde{L}_s$ [*Bhatnagar et al.*, 2008]. We now show that this dependence can also be derived analytically.

[34] The first term in the denominator of equation (41) contains the expression $(\tilde{c}^h_m - c^h_w\ \tilde{c}_{m,sol}\ (\tilde{z}))$, where $\tilde{c}^h_m$ was defined as $\tilde{c}^h_m = c^h_m/c^l_{m,eqb}$, which for most marine systems is of the order of $\tilde{c}^h_m = 0.134/10^{-3} \approx 10^2$ [*Sloan and Koh*, 2007]. The other two terms $c^h_w\ \tilde{c}_{m,sol}\ (\tilde{z})$ and $\tilde{c}'_{m,sol}\ (\tilde{z})$ are usually less than unity. This implies that $\tilde{c}^h_m$ will be about two orders in magnitude greater than the other terms in the denominator and this approximation helps us to simplify equation (41):

$$S_h \approx \frac{\left(\frac{f_{CH_4}-Q\tilde{c}_{m,sol}(\tilde{z})}{\left(\frac{1+\gamma\tilde{\phi}}{\gamma}\right)}\right)+\tilde{c}'_{m,sol}(\tilde{z})}{\frac{Pe_1\tilde{U}_s}{1-\tilde{\phi}}\frac{1+\gamma}{\gamma}\tilde{\rho}_h\tilde{c}^h_m}, 1-\tilde{L}_h<\tilde{z}<1, \quad (45)$$

which can be written in terms of the product $Pe_1S_h$:

$$Pe_1S_h \approx \frac{\left(\frac{f_{CH_4}-Q\tilde{c}_{m,sol}(\tilde{z})}{\left(\frac{1+\gamma\tilde{\phi}}{\gamma}\right)}\right)+\tilde{c}'_{m,sol}(\tilde{z})}{\frac{\tilde{U}_s}{1-\tilde{\phi}}\frac{1+\gamma}{\gamma}\tilde{\rho}_h\tilde{c}^h_m}, 1-\tilde{L}_h<\tilde{z}<1. \quad (46)$$

Equation (46) can be integrated over depth of the GHSZ and divided by the depth of GHSZ, noting that the normalized depth of the GHSZ is unity, to give the term $Pe_1\langle S_h\rangle$, the average gas hydrate flux in the GHSZ:

$$Pe_1\langle S_h\rangle \approx \int_{1-\tilde{L}_h}^{1}\frac{\left(\frac{f_{CH_4}-Q\tilde{c}_{m,sol}(\tilde{z})}{\left(\frac{1+\gamma\tilde{\phi}}{\gamma}\right)}\right)+\tilde{c}'_{m,sol}(\tilde{z})}{\frac{\tilde{U}_s}{1-\tilde{\phi}}\frac{1+\gamma}{\gamma}\tilde{\rho}_h\tilde{c}^h_m}d\tilde{z}. \quad (47)$$

As mentioned previously, the above equations are only valid for the minimum value of $Pe_1$ given in equation (44). This limit ensures that hydrate saturation predicted by equations (41) and (45) remains less than unity.

### 3.8. Maximum SMT Depth for a Given System

[35] An assumption in the equations derived above is that gas hydrate exists within the GHSZ and, at steady state conditions, extends to the base of the GHSZ. However, if the upward methane flux is low, the pore water methane concentration might not exceed the local solubility, which will result in no gas hydrate formation. This situation is depicted schematically in Figure 2, which compares methane and sulfate concentration profiles for two distinct methane fluxes. For relatively low fluxes (dashed set of curves), methane concentration does not exceed local solubility anywhere within the GHSZ, so no gas hydrate forms. Importantly, though, a finite SMT still exists. Progressively increasing the methane flux from depth will cause methane concentrations to approach the solubility curve. For a certain methane flux, the methane concentration equals that on the solubility curve at some depth within the GHSZ. This case, depicted by the solid set of curves (Figure 2), corresponds to the minimum methane flux required to form gas hydrates. Any methane flux, greater than this minimum, will have an SMT, as well as finite gas hydrate saturation within the GHSZ.

[36] Gas hydrate systems sourced by deeper methane are characterized by a minimum flux required to form gas hydrates, with the actual value dependent on the solubility curve and the methane concentration of the rising fluids. This indirectly imposes a maximum SMT depth for gas hydrate to precipitate ($\tilde{L}_{s,\max}$), as well as a minimum thickness between the top occurrence of gas hydrate and the base of the GHSZ ($\tilde{L}_{h,\min}$) (Figure 2). Notably, the latter is valid only when the observed SMT is shallower than $\tilde{L}_{s,\max}$. Therefore, at steady state, there are two possibilities: (1) the SMT exceeds $\tilde{L}_{s,\max}$, no gas hydrates form, and $\tilde{L}_{h,\min}$ is zero, or (2) $\tilde{L}_{s,\max}$ exceeds the SMT, gas hydrates are present, and $\tilde{L}_{h,\min}$ has a finite value. We focus on the latter case.

[37] Gas hydrates start to precipitate when the methane concentration curve becomes equal to the solubility curve, which can be mathematically imposed by requiring the two curves to become tangential to each other. If we assume this occurs at depth $\tilde{z} = 1 - \tilde{L}_{h,\min}$, it defines the minimum thickness between the top occurrence of gas hydrate and the base of the GHSZ. The following two conditions can then be imposed:

$$\tilde{c}_m^l\Big|_{\tilde{z}=1-\tilde{L}_{h,\min}} = \tilde{c}_{m,sol}\Big|_{\tilde{z}=1-\tilde{L}_{h,\min}}, \text{ and} \tag{48}$$

$$\frac{d\tilde{c}_m^l}{d\tilde{z}}\Big|_{dz=1-\tilde{L}_{h,\min}} = \frac{d\tilde{c}_{m,sol}}{d\tilde{z}}\Big|_{\tilde{z}=1-\tilde{L}_{h,\min}}. \tag{49}$$

Using expressions for concentration profiles and fluxes derived earlier, the above conditions can be recast into the following set of nonlinear equations (section A3):

$$1 - \exp\left(\tilde{D}_s \ln\left(\frac{1+m\tilde{c}_{m,ext}}{m\tilde{c}_{m,ext}}\right)\frac{g\left(1-\tilde{L}_{h,\min}\right) - g\left(\tilde{L}_{s,\max}\right)}{g(0) - g\left(\tilde{L}_{s,\max}\right)}\right) - \frac{\tilde{c}_{m,sol}\Big|_{\left(1-\tilde{L}_{h,\min}\right)}}{\tilde{c}_{m,ext}} = 0 \tag{50}$$

$$\left[\frac{\tilde{D}_s \ln\left(\frac{1+m\tilde{c}_{m,ext}}{m\tilde{c}_{m,ext}}\right) g'\left(1-\tilde{L}_{h,\min}\right)}{g(0) - g\left(\tilde{L}_{s,\max}\right)}\right] \cdot \exp\left(\tilde{D}_s \ln\left(\frac{1+m\tilde{c}_{m,ext}}{m\tilde{c}_{m,ext}}\right)\frac{g\left(1-\tilde{L}_{h,\min}\right) - g\left(\tilde{L}_{s,\max}\right)}{g(0) - g\left(\tilde{L}_{s,\max}\right)}\right) + \frac{\tilde{c}'_{m,sol}\Big|_{\left(1-\tilde{L}_{h,\min}\right)}}{\tilde{c}_{m,ext}} = 0, \tag{51}$$

where $g'(\tilde{z})$ represents the derivative of the function $g(\tilde{z})$, the depth $\tilde{L}_{s,\max}$ corresponds to the maximum SMT depth at tangency, and $\tilde{c}_{m,ext}$ is the normalized methane concentration in the external fluid.

[38] The above set of equations contain two unknowns, $\tilde{L}_{h,\min}$ and $\tilde{L}_{s,\max}$, in terms of the two system parameters, $\tilde{c}_{m,sol}(\tilde{z})$ and $\tilde{c}_{m,ext}$. For simplicity, we assume that pore water from depth is saturated with methane so that $\tilde{c}_{m,ext} = 1$. Thus, any gas hydrate setting, characterized its seafloor depth, bottom water temperature, geotherm and solubility curve, will have a maximum $\tilde{L}_s$ ($=\tilde{L}_{s,\max}$) and minimum $\tilde{L}_h$ ($=\tilde{L}_{h,\min}$) required for gas hydrate to be present. Hence, before actual calculations for gas hydrate saturation are performed, the observed SMT depth should be checked to see whether hydrates should exist or not.

### 3.9. Normalized Methane Solubility Curve

[39] An important parameter in our model is methane solubility within the GHSZ. It can be

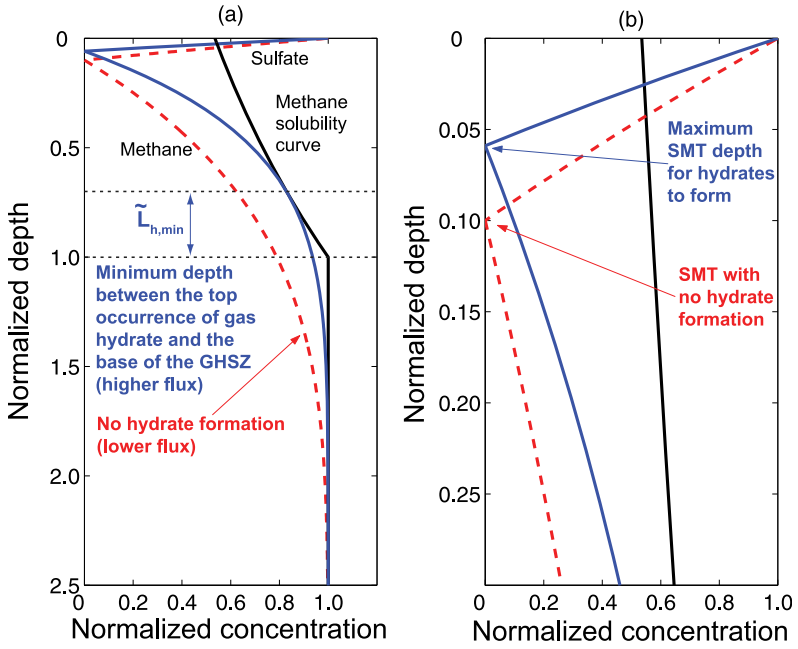


**Figure 2.** (a) Schematic representation of a gas hydrate system showing effect of upward fluid fluxes on pore water sulfate and methane concentration profiles. The solid curves represent the minimum flux case for which the methane concentration just exceeds the local solubility curve, causing hydrates to form. Any fluid flux lower than this minimum value (dashed curves) will not be able to exceed the solubility curve or form any gas hydrate, though a relatively deeper SMT will still exist. (b) Close-up of the same plot showing the maximum allowed SMT depth (solid curves) for a given gas hydrate system. The deeper SMT depth (dashed curves) exceeds the maximum allowed value, implying no gas hydrate formation for this case.

calculated for any geologic setting either through rigorous thermodynamic modeling [*Handa*, 1990; *Bhatnagar et al.*, 2007] or empirical relationships [*Davie et al.*, 2004; *Tishchenko et al.*, 2005]. A simple exponential-type dependence of methane solubility on depth has been proposed by *Davie et al.* [2004]. For simplicity, we also approximate the solubility curve $\tilde{c}_{m,sol}(\tilde{z})$ by an exponential function, although more accurate approximations can be used if needed. We start with a simple two parameter solubility function:

$$\tilde{c}_{m,sol}(\tilde{z}) = r_1 e^{r_2 \tilde{z}}, \tag{52}$$

where $r_1$ and $r_2$ are empirical constants. This solubility curve is normalized by methane solubility at the base of the GHSZ, so that it is unity at $\tilde{z} = 1$. This constraint yields

$$r_1 e^{r_2} = 1 \Rightarrow r_1 = e^{-r_2}, \tag{53}$$

which allows us to reduce equation (52) to a single-parameter equation:

$$\tilde{c}_{m,sol}(\tilde{z}) = e^{-r_2(1-\tilde{z})}. \tag{54}$$

This equation (54), with a single fitting parameter, $r_2$, yields very good fits to solubility curves (Figure 3) obtained through rigorous thermodynamic models [e.g., *Bhatnagar et al.*, 2007].

## 3.10. Model Implementation and Approach

[40] Our analytical approach to relate the depth to the SMT with hydrate saturation throughout the GHSZ is a five step process:

[41] 1. Given the local solubility curve $\tilde{c}_{m,sol}(\tilde{z})$ and site-specific parameters ($m$, $\tilde{D}_s$, $\gamma$ and $\eta$), solve equations (50) and (51) to obtain the maximum allowed SMT depth $\tilde{L}_{s,\max}$. If the observed scaled SMT depth, $\tilde{L}_s$, exceeds $\tilde{L}_{s,\max}$, gas hydrate will not form.

[42] 2. If $\tilde{L}_s < \tilde{L}_{s,\max}$, solve coupled equations (38) and (39) to obtain the dimensionless fluid flux, $Q$, and thickness between the top occurrence of gas hydrate and the base of the GHSZ, $\tilde{L}_h$.

[43] 3. Using these values, calculate methane flux, $f_{CH_4}$, from equation (22), (33) or (37).

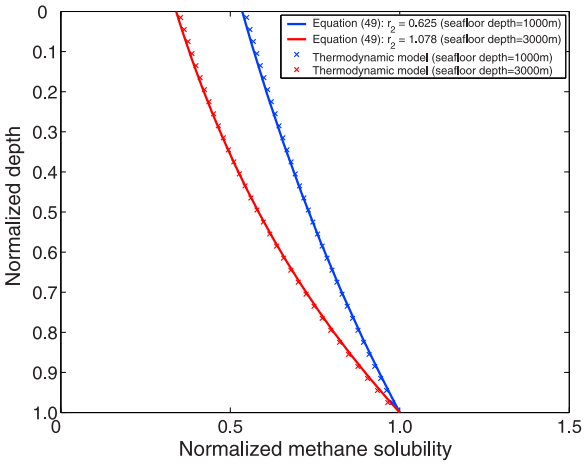


**Figure 3.** Comparison of normalized methane solubility curves, $\tilde{c}_{m,sol}(\tilde{z})$, computed from rigorous thermodynamic models versus those obtained from equation (54). Two different seafloor depths are considered, with the corresponding fitting parameters, $r_2$, listed in the inset. The methane solubility curves correspond to seafloor temperature of 3°C, geotherm of 0.04°C/m, and salinity of 3.5%.

[44] 4. Substitute $Q$, $\tilde{L}_h$, and $f_{CH_4}$ into equations (17) and (34) to get the sulfate and methane concentration profiles.

[45] 5. Use sedimentation rate ($\dot{S}$), porosity inputs $\phi_0$ and $\phi_\infty$ and expressions given in section A1 to find the scaled sediment flux ($\tilde{U}_s$) and fluid flux due to sedimentation ($U_{f,sed}$). Using depth of GHSZ ($L_t$) and methane diffusivity, calculate the first Peclet number, $Pe_1$. Specify $\tilde{\rho}_h$, $\tilde{c}_m^h$ and $c_w^h$, and use equation (41) to define the gas hydrate saturation profile $S_h(\tilde{z})$ within the GHSZ. A simple MATLAB code has been provided with this manuscript as auxiliary material that can be used to do these calculations.[1]

## 4. Results

### 4.1. Relationships Between SMT Depth and Gas Hydrate System Properties

[46] We use our analytical approach to investigate the effects of net methane flux on the scaled SMT depth ($\tilde{L}_s$) and the hydrate saturation profiles The following values are assumed for all calculations and results shown henceforth: $\eta = 6/9$, $\gamma = 9$ (which correspond to $\phi_0 = 0.7$, $\phi_\infty = 0.1$), $c_m^h = 0.134$, $\tilde{\rho}_h = 0.9$, $M_{CH_4} = 16$, $M_{SO_4} = 96$, seawater sulfate concentration equals 28 mM. Methane diffusivity is $0.87 \times 10^{-9}$ m$^2$/s and sulfate diffusivity is $0.56 \times 10^{-9}$ m$^2$/s, which yields a scaled sulfate diffusivity of $\tilde{D}_s = 0.64$ [*Iversen and Jørgensen*, 1993].

[47] Steady state sulfate (Figure 4) and methane (Figure 5) concentration profiles are calculated using equations 17 and 34 for three different scaled SMT depths. Each of these three different scaled SMT depths correspond to a unique net methane flux (Figures 4 and 5). The solubility curve corresponding to seafloor depth of 1000 mbsl ($r_2 = 0.625$) is used for both plots. Due to co-consumption of sulfate and methane at the SMT, shorter $\tilde{L}_s$ indicates higher methane flux from below, thereby leading to a shallower top of the gas hydrate layer (Figure 5).

[48] Gas hydrate saturation profiles as a function of scaled SMT depths show higher gas hydrate saturations within the GHSZ with decreasing $\tilde{L}_s$, again due to net increase in methane flux (Figure 6). Increase in the thickness of the hydrate layer with decreasing $\tilde{L}_s$ is also evident from the saturation profiles. Comparisons between these steady state gas hydrate saturation profiles with previous simulation results [*Bhatnagar et al.*, 2008] indicate consistency between our analytical and numerical formulations. The profiles clearly highlight that each distinct value of $\tilde{L}_s$ results in a unique profile for dissolved sulfate, methane and gas hydrate saturation (Figures 4, 5, and 6).

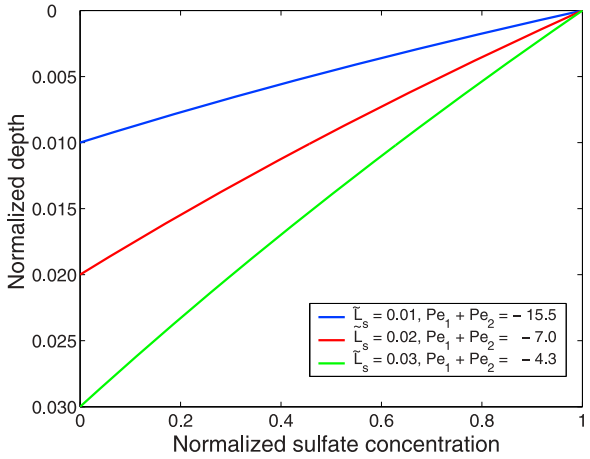


**Figure 4.** Normalized sulfate concentration profiles, obtained through equation (17), for three distinct SMT depths ($\tilde{L}_s$). Sulfate concentration is scaled by its seawater value that makes it equal to unity at the seafloor. Shallower SMT depths indicate higher net methane fluxes from depth. The methane solubility curve corresponds to seafloor depth of 1000 m, seafloor temperature of 3°C, and geotherm of 0.04°C/m.

[1] Auxiliary materials are available in the HTML. doi:10.1029/2010GC003397.

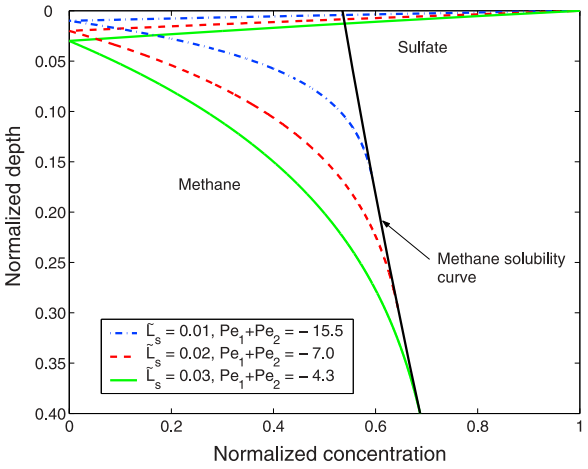


**Figure 5.** Effect of different SMT depths on steady state methane concentration profiles. The sulfate concentration profiles from Figure 4 are also shown for reference. Specifying the scaled SMT depth, $\tilde{L}_s$, uniquely constrains the sulfate and methane concentration profiles, as well as the top of the gas hydrate layer (intersection of the methane concentration profile with the solubility curve). Lower values of $\tilde{L}_s$ imply faster depletion of sulfate due to higher methane flux from below, causing shallower occurrence of the top of the gas hydrate layer. The methane solubility curve corresponds to seafloor depth of 1000 m, seafloor temperature of 3°C, and geotherm of 0.04°C/m.

[49] The downward flux of solid gas hydrate ($Pe_1$ $\langle S_h \rangle$) also relates to $\tilde{L}_s$ (equation 47). This relationship holds for different seafloor depths (Figure 7). Basically, higher values of $Pe_1$ $\langle S_h \rangle$, due to higher net methane input to the system corresponds to decrease (shallowing) in scaled SMT depth ($\tilde{L}_s$). The curves (Figure 7) truncate at a maximum scaled SMT depth ($\tilde{L}_{s,\max}$), beyond which the methane flux is too low to form any gas hydrate. Solubility curves corresponding to seafloor depths of 1000 mbsl and 3000 mbsl result in $\tilde{L}_{s,\max}$ equal to 0.059 and 0.058, respectively. Our analytical model results match well with simulations performed for the same set of parameters by *Bhatnagar et al.* [2008].

## 4.2. Depth Ratio Between Top of Gas Hydrate and the SMT

[50] Several studies have noted a correlation between the SMT depth and the depth to the shallowest occurrence of gas hydrate [e.g., *Borowski et al.*, 1999; *Paull et al.*, 2005; *Bhatnagar et al.*, 2008]]. From a modeling perspective, this should occur because the upward methane flux drives both parameters [*Bhatnagar et al.*, 2008]. *Paull et al.* [2005] suggested that the uppermost gas hydrate might occur at a depth 10 times the SMT depth. Our model allows estimation of this ratio, expressed as $[(L_t - L_h)/L_s]$, or $[(1 - \tilde{L}_h)/\tilde{L}_s]$. This ratio is shown (Figure 8) as a function of scaled SMT depth ($\tilde{L}_s$) for the two solubility curves (same as shown in Figure 3). Overall, the ratio increases with decreasing scaled SMT depth ($\tilde{L}_s$). The ratio increases rapidly for small values of $\tilde{L}_s$, and the variation is more gradual at relatively larger values of $\tilde{L}_s$. With increasing methane flux from below, the SMT migrates upward faster than the increase in thickness between the top occurrence of gas hydrate and the base of the GHSZ ($\tilde{L}_h$).

[51] A key point: except at sites with gas venting or neighboring conduits with rapid fluid flow, the scaled SMT depth at most gas hydrate settings likely exceeds 0.01. This supports the idea that the shallowest gas hydrate lies at about 10–12 times the SMT depth [e.g., *Paull et al.*, 2005].

## 4.3. Application to Cascadia Margin Sites

[52] Cascadia Margin is an accretionary margin characterized by pervasive upward fluid flow with localized gas venting [*Tréhu et al.*, 2004; *Riedel et al.*, 2006]. Results from Ocean Drilling Program Leg 204 and Integrated Ocean Drilling Program

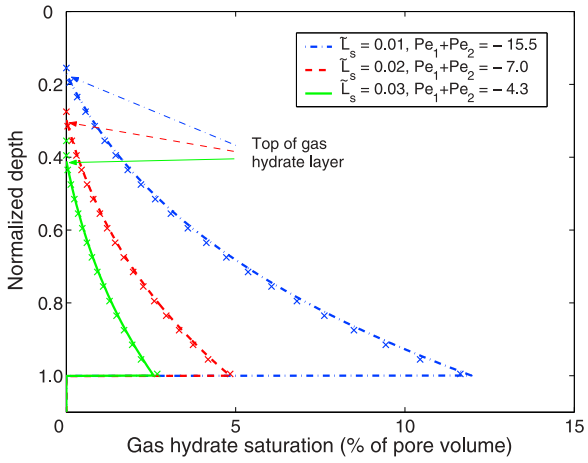


**Figure 6.** Effect of variable SMT depths (same as in Figures 4 and 5) on steady state gas hydrate saturation profiles. Shallower SMT depths, indicating higher net methane flux from depth, result in higher gas hydrate saturations within the GHSZ. Calculation of gas hydrate saturation profile requires specification of $Pe_1$, which was set equal to 0.1 for all three cases. Numerical simulation results (crosses) from the model of *Bhatnagar et al.* [2008] match well with the analytical saturation profiles (curves). Methane solubility curve used is the same as in Figures 4 and 5.

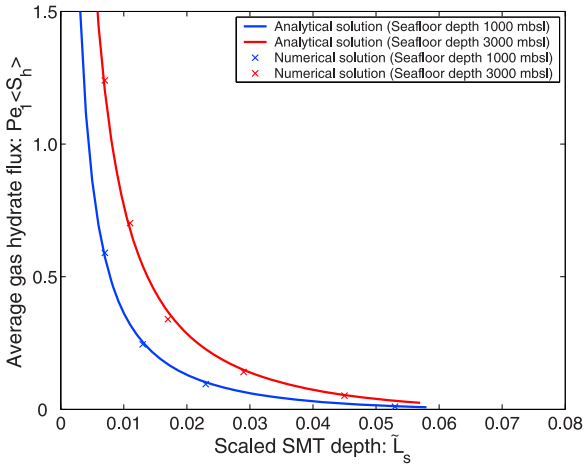


**Figure 7.** Relationship between average gas hydrate flux ($Pe_1\langle S_h\rangle$) and scaled SMT depth ($\tilde{L}_s$) for different seafloor depths of 1000 mbsl and 3000 mbsl (same solubility curves as in Figure 3). Curves representing analytical solutions are also compared with steady state numerical simulations of *Bhatnagar et al.* [2008]. Shallow SMT depths indicate higher methane flux from deeper sources causing higher average gas hydrate flux (and saturations) through the GHSZ.

Expedition 311 provide insight into the complex and heterogeneous gas hydrate distribution at several sites along this margin [*Tréhu et al.*, 2003, 2004; *Riedel et al.*, 2006]. Cascadia Margin sites are characterized by relatively high fluid fluxes and low average total organic carbon (TOC) content [*Westbrook et al.*, 1994; *Riedel et al.*, 2006], which are indicative of a gas hydrate setting where fluids from depth dominate methane supply. This makes sites along Cascadia Margin a good location to test our model. We use SMT depths and site specific data (e.g., sedimentation rate, BSR depth) at four Cascadia Margin sites (Table 1) to predict gas hydrate saturations (average and with depth) and depth to the first occurrence of gas hydrate (Table 2). For each site, the methane solubility curve is generated for the corresponding seafloor conditions using a rigorous thermodynamic model [*Bhatnagar et al.*, 2007]. These calculations also give $c^l_{m,eqb}$ for each site, from which the constant $m$ can be computed. The generated solubility curve is then fit to equation (54) to give the fitting constant $r_2$.

[53] Using the sedimentation rate and porosity, the first Peclet number ($Pe_1$) is computed for each site (equation (4)) (Table 2). The ratio of the dimensional depths $L_s$ and $L_t$ gives the scaled SMT depth $\tilde{L}_s$ (Table 2). With this value, and other site-specific parameters (Table 1), the maximum SMT depth for hydrates to form ($\tilde{L}_{s,\max}$) is computed (Table 2). Solution of equations (38) and (39) gives methane flux and thickness of the gas hydrate layer from which the scaled depth to the first occurrence of gas hydrate ($1 - \tilde{L}_h$) is calculated. Multiplying this by $L_t$ yields the dimensional depth to the first occurrence of hydrate ($L_t - L_h$). The values at Sites U1325 and U1326 (Table 2) compare favorably with those determined from well-log resistivity records [*Malinverno et al.*, 2008].

[54] Using the $Pe_1$ characteristic for each site, we next compute the gas hydrate saturation profile (equation (41)). These are shown for three sites (Figure 9). A profile for Site U1329 is not shown, because our model predicts zero gas hydrate at this location. Averages of these gas hydrate saturation profiles over the entire GHSZ, as well as the gas hydrate occurrence zone (GHOZ), are also computed.

[55] Relevant data at Site 889 has been modeled as a gas hydrate system dominated by a deeper methane source [*Davie and Buffett*, 2003a; *Bhatnagar et al.*, 2007]. *Davie and Buffett* [2003a] used a numerical model to explain the measured pore water chloride profile at this site with equations that included ones describing methane fluxes and the formation, burial and dissociation of gas hydrate. Their results indicate peak hydrate saturation close to 2% at the base

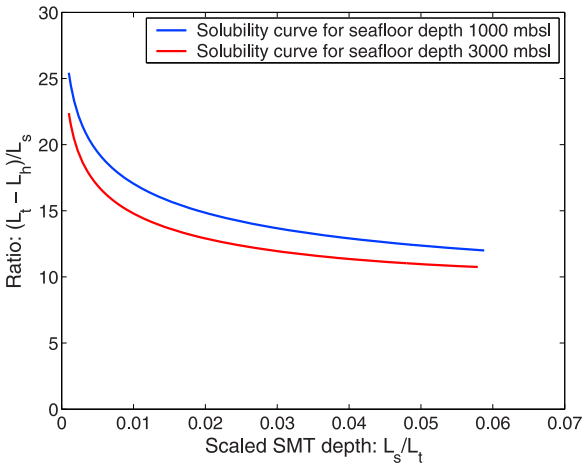


**Figure 8.** Relationship between the ratio of depth to the first occurrence of gas hydrate ($L_t - L_h$) to the SMT depth as a function of the scaled SMT depth for two different solubility curves (Figure 3). This ratio is close to 10–12 for relatively large SMT depths but significantly departs from this suggested range for shallower SMT depths. Similar to Figure 7, both curves truncate at the maximum allowed SMT depth for each case.

**Table 1.** Site-Specific Parameters for Cascadia Margin Sites

| Site | $\dot{S}$ (cm/kyr) | $T_0$ (°C) | $G$ (°C/m) | $D_0$ (m) | $L_s$ (m) | $L_t$ (m) | $c^l_{m,eqb}$ [a] | $m$ (Equation (21)) | $r_2$ [b] (Equation (54)) |
|---|---|---|---|---|---|---|---|---|---|
| 889[c] | 25 | 3 | 0.054 | 1311 | 10 | 225 | $2.1 \times 10^{-3}$ | 4.4 | 0.73 |
| U1325[d] | 38.3 | 3 | 0.06 | 2195 | 5 | 230 | $2.5 \times 10^{-3}$ | 5.2 | 0.93 |
| U1326[d] | 38.3[e] | 3 | 0.06 | 1828 | 2.5 | 230 | $2.3 \times 10^{-3}$ | 4.8 | 0.86 |
| U1329[d] | 9.2 | 3.3 | 0.072 | 946 | 9.4 | 126 | $1.8 \times 10^{-3}$ | 3.8 | 0.52 |

[a]Calculated from thermodynamic model [*Bhatnagar et al.*, 2007].
[b]Calculated from fitting equation (54) to solubility curves obtained from thermodynamic model [*Bhatnagar et al.*, 2007].
[c]ODP Leg 146 [*Westbrook et al.*, 1994].
[d]IODP Expedition 311 [*Riedel et al.*, 2006].
[e]$\dot{S}$ was not available, hence assumed equal to rate at the nearest site U1325.

of GHSZ, and average saturation <1% within the GHSZ [*Davie and Buffett*, 2003a]. This result agrees favorably with our simulation that shows peak saturation of about 2.2% at the base of GHSZ (Figure 9) and average saturation of 0.4% and 0.9% across the entire GHSZ and GHOZ respectively (Table 2). Initially, gas hydrate saturations of 25–30% of pore space for the 100 m above the base of GHSZ at Site 889 were calculated from pore water chloride and resistivity log data [*Yuan et al.*, 1996; *Hyndman et al.*, 1999]. However, subsequent calculations have lowered this estimate considerably. Using a different set of Archie parameters for the resistivity data, a gas hydrate saturation of 5–10% was calculated for the same 100 m interval [*Collett*, 2000]. *Ussler and Paull* [2001] showed that if in situ chloride concentrations smoothly decreased with depth (rather than being equal to those of seawater), gas hydrate saturation was 2–5%, and only within discrete layers. Temperature measurements of cores also indicate hydrate saturation of about 3% at Site 889 [*Kastner et al.*, 1995]. Uncertainties in the amount and distribution of gas hydrate will remain at this location because of the limited scope of information collected compared to subsequent drilling legs targeting gas hydrate [*Riedel et al.*, 2006]. Nonetheless, average gas hydrate saturation predicted at Site 889 using our SMT based model concurs with the lower estimates.

[56] For IODP Expedition 311 sites, average gas hydrate saturations can be computed from chloride anomalies [*Egeberg and Dickens*, 1999; *Paull et al.*, 2005], and resistivity log data using the Archie equation and parameters [*Riedel et al.*, 2006] (Table 2). From the field data, we estimate average gas hydrate saturations over the GHSZ to be 3.7% and 5.3% at Site U1325, and 6.7% and 5.5% at Site U1326 [*Riedel et al.*, 2006; *Bhatnagar et al.*, 2008]. Our SMT based model estimates average gas hydrate saturation across the entire GHSZ to be 1.9% and 4.7% at Sites U1325 and U1326, respectively (Table 2). *Malinverno et al.* [2008] have independently estimated gas hydrate saturations at these locations within the GHOZ using chloride and resistivity logs; they report these as being 3.6 ± 0.6% and 5.6 ± 0.7%, respectively. These values compare favorably with the 2.7% and 5.7% average gas hydrate saturation within the GHOZ determined from our SMT based model (Table 2).

[57] According to our model, the SMT at Site U1329 is deeper than the maximum depth allowed for gas hydrate precipitation; that is, the upward methane flux is sufficiently low such that methane concentrations do not exceed solubility conditions. The prediction of zero gas hydrate at this site corresponds to very low values interpreted from chloride data (0.1%), resistivity data (2%), and indepen-

**Table 2.** Results for Cascadia Margin Sites

| Site | $Pe_1$ | $\tilde{L}_s$ | $\tilde{L}_{s,\max}$ | $L_t - L_h$ (m) | Top GHOZ (mbsf) | $\langle S_h \rangle_{GHSZ}$ (calc.) | $\langle S_h \rangle_{GHSZ}$ (res. log) | $\langle S_h \rangle_{GHSZ}$ ($Cl^-$) | $\langle S_h \rangle_{GHOZ}$ (calc.) | $\langle S_h \rangle_{GHOZ}$ (res. log and $Cl^-$) |
|---|---|---|---|---|---|---|---|---|---|---|
| 889[a] | 0.068 | 0.0444 | 0.059 | 121.5 | - | 0.4% | - | <1%[a] | 0.9% | - |
| U1325[b] | 0.11 | 0.0217 | 0.058 | 69.8 | 73[c] | 1.9% | 3.7%[b] | 5.3% | 2.7% | 3.6 ± 0.6%[c] |
| U1326[b] | 0.11 | 0.0108 | 0.060 | 40.9 | 47[c] | 4.7% | 6.7%[b] | 5.5% | 5.7% | 5.6 ± 0.7%[c] |
| U1329[b] | 0.014 | 0.0746 | 0.056 | - | - | 0% | 2%[b] | 0.1% | 0% | 0%[c] |

[a]From fit to chloride data [*Davie and Buffett*, 2003a].
[b]From Archie equation [*Archie*, 1942] using LWD data [*Riedel et al.*, 2006].
[c]From joint interpretation of pore water chlorinity data and LWD logs of porosity and electrical resistivity [*Malinverno et al.*, 2008].

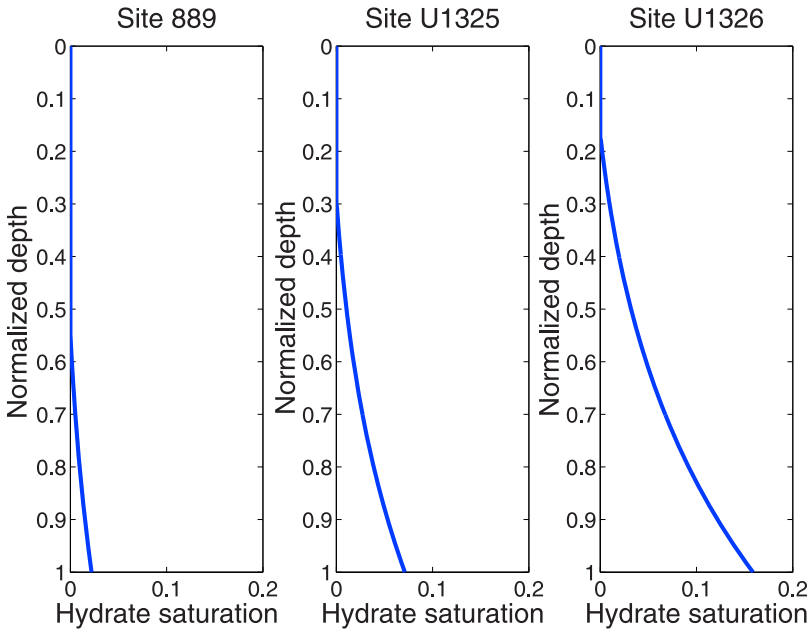


**Figure 9.** Steady state gas hydrate saturation profiles computed from scaled SMT depths at Cascadia Margin Sites 889, U1325, and U1326. Scaled SMT depth is highest for Site 889 and lowest for Site U1326, implying higher methane flux and greater gas hydrate saturation at Site U1326 and relatively low methane flux and hydrate saturation at Site 889.

dent estimation (0%) by *Malinverno et al.* [2008] (Table 2). Moreover, no gas hydrate was recovered from cores at this site. Site U1329 is interpreted to mark the eastern limit of gas hydrate occurrence in this region [*Riedel et al.*, 2006].

[58] In general, we get good first-order agreement between average gas hydrate saturations interpreted from resistivity logs and chloride anomalies and those predicted using our model. However, our model consistently predicts lower average saturation at all four sites examined. This deviation certainly could reflect assumptions and simplifications in our modeling; it could also reflect problems in measuring gas hydrate abundance. For example, estimates from resistivity logs depend on knowledge regarding formation water resistivity and three empirical constants, which are difficult to constrain in clay-rich sediments [*Cook and Goldberg*, 2008; *Lee and Collett*, 2009]. Moreover, and without any mechanistic rationale, log-based results often show the first gas hydrate to occur near the seafloor, where there is insufficient methane. The latter would cause gas hydrate saturations to be higher than those predicted from transport models. Similarly, estimation of gas hydrate saturation from chloride data is quite sensitive to the choice of background chloride concentrations [*Ussler and Paull*, 1995; *Egeberg and Dickens*, 1999]. Apart from the relatively small deviations, our model gives a good estimate for average gas hydrate saturation and for the top occurrence of gas hydrate. Further, our approach captures both the variation in average gas hydrate saturation and the thickness of gas hydrate across the IODP Expedition 311 transect. Likely, it also provides a lower bound on average gas hydrate saturation at Site 889.

## 5. Caveats

[59] Our analytical approach provides a simple tool to estimate the amount and occurrence of gas hydrate at sites dominated by a relatively high upward flux of methane. Compared to full-scale, numerical simulations, this method gives a quick, accurate, first-order estimate of gas hydrate saturation and the top occurrence of gas hydrate. However, some caveats should be noted before application.

[60] 1. The analysis only applies to gas hydrate systems where AOM across the SMT drives net consumption of sulfate in shallow sediment. If organoclastic reduction in shallow sediment removes significant amounts pore water sulfate, the resulting SMT will become shallower than by the upward methane flux alone. In such cases, our method will

predict gas hydrate saturations higher than those existing in the sediment.

[61] 2. The approach assumes that methane is the only hydrocarbon. In some regions (e.g., Gulf of Mexico), the upward fluid flux might contain significant amounts of other hydrocarbons (e.g., higher alkanes), which might react with sulfate [*Joye et al.*, 2004]. This would invalidate the 1:1 sulfate-methane flux relationship. Such sites might be more appropriately characterized by a sulfate-hydrocarbon transition [*Castellini et al.*, 2006] and modeled accordingly.

[62] 3. The methodology applies to systems that can be considered one dimensional. Sites dominated by lateral fluid migration, focused fluid flow through high permeability conduits, or both, will probably show greater deviations between gas hydrate saturation estimated from our model and that inferred from other proxy data (e.g., resistivity, chloride).

[63] 4. The formulation gives first-order estimates for gas hydrate abundance, but cannot predict small-scale heterogeneities in gas hydrate saturation. Geophysical and geochemical proxies often suggest a heterogeneous distribution of gas hydrate within the GHSZ, probably controlled by local variations in lithology [e.g., *Malinverno*, 2010].

[64] 5. The model does not account for the existence or migration of free gas within the GHSZ. Several sites have been drilled at or near locations of seafloor gas venting, including along Cascadia Margin (Sites 1249 and 1250, ODP Leg 204) [*Tréhu et al.*, 2003]; Site U1328 [*Riedel et al.*, 2006]). These sites have layers containing massive gas hydrate close to the seafloor, which may have precipitated from free gas [*Haeckel et al.*, 2004]. Gas hydrate saturation at such sites appears to decrease with depth below the seafloor [*Milkov et al.*, 2004; *Liu and Flemings*, 2006; *Riedel et al.*, 2006], opposite to that generated in our model and others [*Xu and Ruppel*, 1999; *Davie and Buffett*, 2001; *Bhatnagar et al.*, 2007, 2008].

[65] 6. The approach assumes long-term steady state conditions, something that is difficult to assess [*Dickens*, 2001]. Previously, we have shown details of transient simulations [*Bhatnagar et al.*, 2008], which require more complex numerical modeling. A main objective of this paper is to provide quick results without the associated mathematical and computational complexity. To this end, we have stated all our steady state assumptions and the limitations of this approach.

[66] 7. The method requires accurate pore water sulfate profiles above and across the SMT. Although obvious, this point needs emphasis because sometimes coring can lead to incomplete or duplicate sediment records. As a noteworthy example, the top 2–3 m were not recovered at Hole U1325B, such that the SMT appears to occur at <2.5 mbsf instead of at 5.0 mbsf [*Riedel et al.*, 2006]. Use of the wrong SMT depth [*Torres and Kastner*, 2009] would lead to incorrect inferences, specifically a greater gas hydrate abundance and a shallower top occurrence of gas hydrate than we have modeled or which was documented at this site.

## 6. Conclusions

[67] We develop analytical expressions to estimate gas hydrate saturation from the sulfate-methane transition (SMT) for gas hydrate systems that have a relatively high (but not focused) upward methane flux. Using simple one-dimensional mass balances for sulfate and methane, we show that net methane flux in such "deep-sourced" systems uniquely determines the SMT depth, the thickness of the gas hydrate layer, and gas hydrate saturation within the GHSZ. This dependence allows estimation of the vertical extent of gas hydrate and its saturation through knowledge of the SMT depth. Steady state results show that as the SMT becomes shallower, methane flux and, consequently, gas hydrate saturation increases. This has been suggested from field observations and other modeling, but not in terms of coupled mathematical equations for sulfate and methane.

[68] Our formulation gives estimates of the maximum SMT depth and minimum upward methane flux for gas hydrate occurrence in a given setting. When the SMT exceeds this depth, the flux is too low to deliver sufficient methane to form gas hydrate. The direct relationship between SMT depth and the thickness of the gas hydrate layer allows us to obtain the depth ratio between the first occurrence of gas hydrate and the SMT. This ratio can be about 10–12 for sites characterized by low to moderate methane fluxes. However, relatively higher methane fluxes will increase this ratio.

[69] Average gas hydrate saturations calculated over the GHSZ at Sites 889, U1325, U1326 and U1329 are 0.4%, 1.9%, 4.7% and 0%, respectively. The predicted top occurrences of gas hydrate for the first three sites are 120, 70, and 40 mbsf, respectively. These values compare favorably with amounts and distributions estimated from resistivity log and chlorinity data. Although our analytical formulation does not give the detailed gas hydrate

distribution at the m scale within the GHOZ, it does provide a simple and fast technique to constrain the gas hydrate saturation profile for systems with a relatively high upward methane flux.

# Appendix A

## A1. Nondimensionalization of Sulfate Mass Balance

[70] The net fluid flux in the system ($U_{f,tot}$) results from the combination of fluid flux due to continuous sedimentation and compaction of sediments ($U_{f,sed}$) and the external fluid flux ($U_{f,ext}$) [*Davie and Buffett*, 2003b; *Bhatnagar et al.*, 2007]:

$$U_{f,tot} = U_{f,sed} + U_{f,ext}. \tag{A1}$$

In terms of Peclet numbers, equation (4), this sum can be written as

$$\frac{U_{f,tot}L_t}{D_m} = \frac{U_{f,sed}L_t}{D_m} + \frac{U_{f,ext}L_t}{D_m} = Pe_1 + Pe_2. \tag{A2}$$

Multiplying equation (3) by $L_t/D_m$ and dividing by $c_{s,o}$ gives

$$(Pe_1 + Pe_2)\tilde{c}_s^l - \phi\frac{D_s}{D_m}\frac{d\tilde{c}_s^l}{d\tilde{z}} = \frac{F_{SO_4}}{\rho_w c_{s,o}}\frac{L_t}{D_m}. \tag{A3}$$

[71] The decrease in porosity with depth is modeled by relating sediment porosity to effective stress, and assuming hydrostatic pressure (equilibrium compaction). This yields the following relationship between reduced porosity and normalized depth [*Bhatnagar et al.*, 2007]:

$$\tilde{\phi} = \frac{\eta}{\eta + (1-\eta)e^{N_{t\phi}\tilde{z}}}, \tag{A4}$$

where $\tilde{\phi}$ and $\eta$ are reduced porosities defined in terms of the maximum ($\phi_0$) and minimum ($\phi_\infty$) porosities achieved during compaction:

$$\tilde{\phi} = \frac{\phi - \phi_\infty}{1-\phi_\infty},\ \eta = \frac{\phi_0 - \phi_\infty}{1-\phi_\infty}. \tag{A5}$$

$N_{t\phi}$ denotes the ratio of the depth to the base of the GHSZ to the characteristic length of compaction ($L_\phi$) [*Bhatnagar et al.*, 2007] and is defined as

$$N_{t\phi} = \frac{L_t}{L_\phi}. \tag{A6}$$

Dividing equation (A3) by $(1-\phi_\infty)$ we obtain the dimensionless form of the sulfate mass balance equation (5) of the main text:

$$\left(\frac{1+\gamma}{\gamma}\right)(Pe_1 + Pe_2)\tilde{c}_s^l - \left(\frac{1+\gamma\tilde{\phi}}{\gamma}\right)\frac{D_s}{D_m}\frac{d\tilde{c}_s^l}{d\tilde{z}} = \left(\frac{1}{1-\phi_\infty}\right)\frac{F_{SO_4}}{\rho_w c_{s,o}}\frac{L_t}{D_m}, 0 < \tilde{z} < \tilde{L}_s, \tag{A7}$$

where $\gamma$ was defined in the main text as $\left(\frac{1-\phi_\infty}{\phi_\infty}\right)$.

[72] Sediment and fluid flux expressions in our steady state burial model warrant brief discussion. The fluid flux due to sedimentation and compaction ($U_{f,sed}$) can be expressed as a combination of seafloor sedimentation rate ($\dot{S}$) and defined porosities as follows [*Bhatnagar et al.*, 2007]:

$$U_{f,sed} = \frac{1-\phi_o}{1-\phi_\infty}\dot{S}\phi_\infty. \tag{A8}$$

[73] The sediment flux ($U_s$) can be normalized with respect to the fluid flux caused by sedimentation ($U_{f,sed}$). This normalized sediment flux equals a constant, $\gamma$:

$$\tilde{U}_s = \frac{U_s}{U_{f,sed}} = \frac{\dot{S}(1-\phi_o)}{U_{f,sed}} = \frac{\left(\frac{1-\phi_\infty}{\phi_\infty}\right)U_{f,sed}}{U_{f,sed}} = \frac{1-\phi_\infty}{\phi_\infty} = \gamma. \tag{A9}$$

## A2. Nondimensionalization of Methane Mass Balance

[74] The steady state water mass balance below the SMT can be written as

$$\frac{d}{dz}\left[U_f\rho_w c_w^l + \frac{U_s}{1-\phi}\phi S_h c_w^h \rho_h\right] = 0, L_s < z < L_t, \tag{A10}$$

where $c_w^l$ and $c_w^h$ are the water mass fractions in pore water and hydrate phase, respectively. equation (A10) can also be written in terms of the water flux ($F_{H_2O}$) as

$$U_f\rho_w c_w^l + \frac{U_s}{1-\phi}\phi S_h c_w^h \rho_h = F_{H_2O} = \left(U_{f,sed} + U_{f,ext}\right)\rho_w. \tag{A11}$$

Due to low methane solubility in water, we assume the mass fraction of water in aqueous phase to be unity. This gives us an expression for the water flux:

$$U_f = \left(U_{f,sed} + U_{f,ext}\right) - \frac{U_s}{1-\phi}\phi S_h c_w^h \frac{\rho_h}{\rho_w}. \tag{A12}$$

Substituting this expression for fluid flux into equation (24) gives

$$\left[\left(U_{f,sed}+U_{f,ext}\right)-\frac{U_s}{1-\phi}\phi S_h c_w^h\frac{\rho_h}{\rho_w}\right]c_m^l+\frac{U_s}{1-\phi}\phi S_h c_m^h\frac{\rho_h}{\rho_w}-\phi(1-S_h)D_m\frac{dc_m^l}{dz}=\frac{F_{CH_4}}{\rho_w}. \quad \text{(A13)}$$

Similar to the sulfate mass balance, we multiply the above equation by $L_t/D_m$ and divide by $c^l_{m,eqb}$ to get the following dimensionless form:

$$\left[(Pe_1+Pe_2)-\frac{Pe_1\tilde{U}_s}{1-\phi}\phi S_h c_w^h\tilde{\rho}_h\right]c_m^l+\frac{Pe_1\tilde{U}_s}{1-\phi}\phi S_h\tilde{c}_m^h\tilde{\rho}_h-\phi(1-S_h)\frac{d\tilde{c}_m^l}{d\tilde{z}}=\frac{F_{CH_4}}{\rho_w c^l_{m,eqb}}\frac{L_t}{D_m}, \quad \text{(A14)}$$

where different scaled variables were defined in equation (25). Equation (A14) can be rearranged as

$$(Pe_1+Pe_2)c_m^l+\frac{Pe_1\tilde{U}_s}{1-\phi}\phi S_h\tilde{\rho}_h\left(\tilde{c}_m^h-c_w^h c_m^l\right)-\phi(1-S_h)\frac{d\tilde{c}_m^l}{d\tilde{z}}=\frac{F_{CH_4}}{\rho_w c^l_{m,eqb}}\frac{L_t}{D_m}. \quad \text{(A15)}$$

Finally, dividing by $(1-\phi_\infty)$ to express in terms of the reduced porosity, we get the dimensionless methane balance, equation (26).

## A3. Deriving Conditions for Maximum $\tilde{L}_s$ and Minimum $\tilde{L}_b$

[75] The methane concentration profile in the absence of gas hydrate can be obtained using equation (27) along with the following boundary conditions:

$$\text{B.C. (1)}: \tilde{c}_m^l=0, \text{ at } \tilde{z}=\tilde{L}_s \quad \text{(A16)}$$

$$\text{B.C. (2)}: \tilde{c}_m^l=\tilde{c}_{m,ext}, \text{ at } \tilde{z}=D, \quad \text{(A17)}$$

where $D$ represents the bottom of the domain. These boundary conditions lead to the following methane concentration profile:

$$\tilde{c}_m^l(\tilde{z})=\tilde{c}_{m,ext}\frac{1-\exp\left(Q\left[g(\tilde{z})-g\left(\tilde{L}_s\right)\right]\right)}{1-\exp\left(Q\left[g(D)-g\left(\tilde{L}_s\right)\right]\right)}. \quad \text{(A18)}$$

If the depth of the external boundary condition ($D$) is sufficiently greater than unity, the exponential function in the denominator of the above expression approaches zero, simplifying the methane concentration profile and the methane flux as follows:

$$\tilde{c}_m^l(\tilde{z})=\tilde{c}_{m,ext}\left(1-\exp\left(Q\left[g(\tilde{z})-g\left(\tilde{L}_s\right)\right]\right)\right), D>>1 \quad \text{(A19)}$$

$$f_{CH_4}=Q\tilde{c}_{m,ext}. \quad \text{(A20)}$$

Equating this methane flux to the sulfate flux at the SMT using equations (14) and (22) yields:

$$(-m)Q\tilde{c}_{m,ext}=\frac{Q}{1-\exp\left(\frac{Q}{\tilde{D}_s}\left[g(0)-g\left(\tilde{L}_s\right)\right]\right)}. \quad \text{(A21)}$$

The above equation can be used to obtain the dimensionless flux, $Q$, as a function of $\tilde{L}_s$:

$$Q=\frac{\tilde{D}_s\ln\left(\frac{1+m\tilde{c}_{m,ext}}{m\tilde{c}_{m,ext}}\right)}{g(0)-g\left(\tilde{L}_s\right)}. \quad \text{(A22)}$$

Finally, substituting the above relationship and equation (A19) into the tangency conditions (48) and (49) gives the coupled set of equations (50) and (51).

## Acknowledgments

[76] We acknowledge financial support from the Shell Center for Sustainability, the Kobayashi Graduate Fellowship, and the Department of Energy (DE-FC26-06NT42960). We thank the captains, crews, and scientists aboard during ODP Leg 146 and IODP Leg 311, which provided the data that enabled us to frame and evaluate our models. We also thank Editor Louis Derry and two anonymous reviewers for their constructive and critical commentaries on this paper.

## References

Archer, D., B. A. Buffett, and V. Brovkin (2009), Ocean methane hydrates as a slow tipping point in the global carbon cycle, *Proc. Natl. Acad. Sci. U. S. A.*, *106*(49), 20,596–20,601, doi:10.1073/pnas.0800885105.

Archie, G. E. (1942), The electrical resistivity log as an aid in determining some reservoir characteristics, *Trans. Am. Inst. Min. Metall. Pet. Eng.*, *146*, 54–62.

Berner, R. A. (1980), *Early Diagenesis: A Theoretical Approach*, Princeton Univ. Press, Princeton, N. J.

Bhatnagar, G., W. G. Chapman, G. R. Dickens, B. Dugan, and G. J. Hirasaki (2007), Generalization of gas hydrate distribution and saturation in marine sediments by scaling of thermodynamic and transport processes, *Am. J. Sci.*, *307*, 861–900, doi:10.2475/06.2007.01.

Bhatnagar, G., W. G. Chapman, G. R. Dickens, B. Dugan, and G. J. Hirasaki (2008), Sulfate-methane transition as a proxy for

average methane hydrate saturation in marine sediments, *Geophys. Res. Lett.*, *35*, L03611, doi:10.1029/2007GL032500.

Borowski, W. S., C. K. Paull, and W. Ussler III (1996), Marine pore water sulfate profiles indicate in situ methane flux from underlying gas hydrate, *Geology*, *24*(7), 655–658, doi:10.1130/0091-7613(1996)024<0655:MPWSPI>2.3.CO;2.

Borowski, W. S., C. K. Paull, and W. Ussler III (1999), Global and local variations of interstitial sulfate gradients in deep-water, continental margin sediments: Sensitivity to underlying methane and gas hydrates, *Mar. Geol.*, *159*, 131–154, doi:10.1016/S0025-3227(99)00004-3.

Boudreau, B. P., and J. T. Westrich (1984), The dependence of bacterial sulfate reduction on sulfate concentration in marine sediments, *Geochim. Cosmochim. Acta*, *48*, 2503–2516, doi:10.1016/0016-7037(84)90301-6.

Briaud, J. L., and A. Chaouch (1997), Hydrate melting in soil around hot conductor, *J. Geotech. Geoenviron. Eng.*, *123*, 645–653, doi:10.1061/(ASCE)1090-0241(1997)123:7(645).

Castellini, D. G., G. R. Dickens, G. T. Snyder, and C. D. Ruppel (2006), Barium recycling in shallow sediment above active mud volcanoes in the Gulf of Mexico, *Chem. Geol.*, *226*, 1–30, doi:10.1016/j.chemgeo.2005.08.008.

Collett, T. S. (2000), Quantitative well-log analysis of in-situ natural gas hydrates, Ph.D. dissertation, Colo. School of Mines, Golden, Colo.

Collett, T. S. (2002), Energy resource potential of natural gas hydrates, *AAPG Bull.*, *86*, 1971–1992.

Cook, A. E., and D. Goldberg (2008), Extent of gas hydrate filled fracture planes: Implications for in situ methanogenesis and resource potential, *Geophys. Res. Lett.*, *35*, L15302, doi:10.1029/2008GL034587.

Davie, M. K., and B. A. Buffett (2001), A numerical model for the formation of gas hydrate below the seafloor, *J. Geophys. Res.*, *106*, 497–514, doi:10.1029/2000JB900363.

Davie, M. K., and B. A. Buffett (2003a), Sources of methane for marine gas hydrate: Inferences from a comparison of observations and numerical models, *Earth Planet. Sci. Lett.*, *206*, 51–63, doi:10.1016/S0012-821X(02)01064-6.

Davie, M. K., and B. A. Buffett (2003b), A steady state model for marine hydrate formation: Constraints on methane supply from pore water sulfate profiles, *J. Geophys. Res.*, *108*(B10), 2495, doi:10.1029/2002JB002300.

Davie, M. K., O. Y. Zatsepina, and B. A. Buffett (2004), Methane solubility in marine hydrate environments, *Mar. Geol.*, *203*, 177–184, doi:10.1016/S0025-3227(03)00331-1.

Dickens, G. R. (2001), Sulfate profiles and barium fronts in sediment on the Blake Ridge: Present and past methane fluxes through a large gas hydrate reservoir, *Geochim. Cosmochim. Acta*, *65*, 529–543, doi:10.1016/S0016-7037(00)00556-1.

Dickens, G. R. (2003), Rethinking the global carbon cycle with a large, dynamic and microbially mediated gas hydrate capacitor, *Earth Planet. Sci. Lett.*, *213*, 169–183, doi:10.1016/S0012-821X(03)00325-X.

Dickens, G. R., and G. T. Snyder (2009), Interpreting upward methane flux, *Fire in the Ice, Winter*, 7–10.

Egeberg, P. K., and G. R. Dickens (1999), Thermodynamic and pore water halogen constraints on hydrate distribution at ODP Site 997(Blake Ridge), *Chem. Geol.*, *153*, 53–79, doi:10.1016/S0009-2541(98)00152-1.

Haeckel, M., E. Suess, K. Wallman, and D. Rickert (2004), Rising methane gas bubbles form massive hydrate layers at the seafloor, *Geochim. Cosmochim. Acta*, *68*, 4335–4345, doi:10.1016/j.gca.2004.01.018.

Handa, Y. P. (1990), Effect of hydrostatic pressure and salinity on the stability of gas hydrates, *J. Phys. Chem.*, *94*, 2652–2657, doi:10.1021/j100369a077.

Hensen, C., and K. Wallman (2005), Methane formation at Costa Rica continental margin constraints for gas hydrate inventories and cross-décollement fluid flow, *Earth Planet. Sci. Lett.*, *236*, 41–60, doi:10.1016/j.epsl.2005.06.007.

Holbrook, W. S., H. Hoskins, W. T. Wood, R. A. Stephen, D. Lizzaralde, and the Leg 164 Science Party (1996), Methane hydrate and free gas on the Blake Ridge from vertical seismic profiling, *Science*, *273*, 1840–1843, doi:10.1126/science.273.5283.1840.

Hyndman, R. D., and E. E. Davis (1992), A mechanism for the formation of methane hydrate and seafloor bottom-simulating reflectors by vertical fluid expulsion, *J. Geophys. Res.*, *97*, 7025–7041, doi:10.1029/91JB03061.

Hyndman, R. D., T. Yuan, and K. Moran (1999), The concentration of deep sea gas hydrates from downhole electrical resistivity logs and laboratory data, *Earth Planet. Sci. Lett.*, *172*, 167–177, doi:10.1016/S0012-821X(99)00192-2.

Iversen, N., and B. B. Jørgensen (1993), Diffusion coefficients of sulfate and methane in marine sediments: Influence of porosity, *Geochim. Cosmochim. Acta*, *57*, 571–578, doi:10.1016/0016-7037(93)90368-7.

Joye, S. B., A. Boetius, B. N. Orcutt, J. P. Montoya, H. N. Schulz, M. J. Erickson, and S. K. Lugo (2004), The anaerobic oxidation of methane and sulfate reduction in sediments from Gulf of Mexico cold seeps, *Chem. Geol.*, *205*, 219–238, doi:10.1016/j.chemgeo.2003.12.019.

Kastner, M., K. A. Kvenvolden, M. J. Whiticar, A. Camerlenghi, and T. D. Lorenson (1995), Relation between pore fluid chemistry and gas hydrates associated with bottom-simulating reflectors at the Cascadia Margin, Sites 889 and 892, *Proc. Ocean Drill. Program Sci. Results*, *146*, 175–187.

Kastner, M., M. Torres, E. Solomon, and A. J. Spivack (2008), Marine pore fluid profiles of dissolved sulfate: Do they reflect in situ methane fluxes?, *Fire in the Ice, Summer*, 6–8.

Kvenvolden, K. A. (1993), Gas hydrates: Geological perspective and global change, *Rev. Geophys.*, *31*, 173–187, doi:10.1029/93RG00268.

Kwon, T. H., K. I. Song, and G. C. Cho (2010), Destabilization of marine gas hydrate-bearing sediments induced by a hot wellbore: A numerical approach, *Energy Fuels*, *24*, 5493–5507, doi:10.1021/ef100596x.

Lee, M. W., and T. S. Collett (2009), Gas hydrate saturations estimated from fractured reservoir at Site NGHP-01–10, Krishna-Godavari Basin, India, *J. Geophys. Res.*, *114*, B07102, doi:10.1029/2008JB006237.

Liu, X., and P. B. Flemings (2006), Passing gas through the hydrate stability zone at southern Hydrate Ridge, offshore Oregon, *Earth Planet. Sci. Lett.*, *241*, 211–226, doi:10.1016/j.epsl.2005.10.026.

Luff, R., and K. Wallman (2003), Fluid flow, methane fluxes, carbonate precipitation and biogeochemical turnover in gas hydrate-bearing sediments at Hydrate Ridge, Cascadia Margin: Numerical modeling and mass balances, *Geochim. Cosmochim. Acta*, *67*, 3403–3421, doi:10.1016/S0016-7037(03)00127-3.

Malinverno, A. (2010), Marine gas hydrates in thin sand layers that soak up microbial methane, *Earth Planet. Sci. Lett.*, *292*, 399–408, doi:10.1016/j.epsl.2010.02.008.

Malinverno, A., M. Kastner, M. E. Torres, and U. G. Wortmann (2008), Gas hydrate occurrence from pore water chlorinity and downhole logs in a transect across the northern Cascadia

margin (Integrated Ocean Drilling Program Expedition 311), *J. Geophys. Res.*, *113*, B08103, doi:10.1029/2008JB005702.

Martens, C. S., and R. A. Berner (1974), Methane production in the interstitial waters of sulfate-depleted marine sediments, *Science*, *185*, 1167–1169, doi:10.1126/science.185.4157.1167.

Milkov, A. V., G. R. Dickens, G. E. Claypool, Y. J. Lee, W. S. Borowski, M. E. Torres, W. Xu, H. Tomaru, A. M. Tréhu, and P. Schultheiss (2004), Co-existence of gas hydrate, free gas, and brine within the regional gas hydrate stability zone at Hydrate Ridge (Oregon Margin): Evidence from prolonged degassing of a pressurized core, *Earth Planet. Sci. Lett.*, *222*, 829–843, doi:10.1016/j.epsl.2004.03.028.

Pape, T., S. Kasten, M. Zabel, A. Bahr, F. Abegg, H.-J. Hohnberg, and G. Bohrmann (2010), Gas hydrates in shallow deposits of the Amsterdam mud volcano, Anaximander Mountains, northeastern Mediterranean Sea, *Geo Mar. Lett.*, *30*, 187–206, doi:10.1007/s00367-010-0197-8.

Paull, C. K., W. Ussler III, T. Lorenson, W. Winters, and J. Dougherty (2005), Geochemical constraints on the distribution of gas hydrates in the Gulf of Mexico, *Geo Mar. Lett.*, *25*, 273–280, doi:10.1007/s00367-005-0001-3.

Riedel, M., T. S. Collett, M. J. Malone, and the Expedition 311 Scientists (2006), *Proceedings of the Integrated Ocean Drilling Program Expedition 311*, Integr. Ocean Drill. Program, Washington, D. C.

Sloan, E. D. J., and C. Koh (2007), *Clathrate Hydrates of Natural Gases*, 3rd ed. CRC Press, Boca Raton, Fla.

Snyder, G. T., A. Hiruta, R. Matsumoto, G. R. Dickens, H. Tomaru, R. Takeuchi, J. Komatsubara, Y. Ishida, and H. Yu (2007), Pore water profiles and authigenic mineralization in shallow marine sediments above the methane-charged system on Umitaka Spur, Japan Sea, *Deep Sea Res., Part II*, *54*, 1216–1239, doi:10.1016/j.dsr2.2007.04.001.

Tishchenko, P., C. Hensen, K. Wallman, and C. S. Wong (2005), Calculation of the stability and solubility of methane hydrate in seawater, *Chem. Geol.*, *219*, 37–52, doi:10.1016/j.chemgeo.2005.02.008.

Torres, M. E., and M. Kastner (2009) Data report: Clues about carbon cycling in methane-bearing sediments using stable isotopes of the dissolved inorganic carbon, IODP Expedition 311, in *Cascadia Margin Gas Hydrates*, *Proc. Integr. Ocean Drill. Program*, *311*, doi:10.2204/iodp.proc.311.206.2009.

Tréhu, A. M., G. Bohrmann, F. Rack, and M. E. Torres (Eds.) (2003), *Proceedings of the Ocean Drilling Program*, *Initial Reports*, vol. 204, Ocean Drilling Program, College Station, Tex.

Tréhu, A. M., et al. (2004), Three-dimensional distribution of gas hydrate beneath southern Hydrate Ridge: Constraints from ODP Leg 204, *Earth Planet. Sci. Lett.*, *222*, 845–862, doi:10.1016/j.epsl.2004.03.035.

Tréhu, A. M., C. Ruppel, M. Holland, G. R. Dickens, M. E. Torres, T. S. Collett, D. S. Goldberg, M. Riedel, and P. Schultheiss (2006), Gas hydrates in marine sediments: Lessons from scientific ocean drilling, *Oceanography*, *19*, 124–142.

Ussler, W., and C. K. Paull (1995), Effects of ion exclusion and isotopic fractionation on pore water geochemistry during gas hydrate formation and decomposition, *Geo Mar. Lett.*, *15*, 37–44, doi:10.1007/BF01204496.

Ussler, W., and C. K. Paull (2001), Ion exclusion associated with marine gas hydrate deposits, in *Natural Gas Hydrates: Occurrence, Distribution, and Detection*, *Geophys. Monogr. Ser*, vol. 124, edited by C. K. Paull and W. P. Dillon, pp. 41–51, AGU, Washington, D. C.

Valentine, D. L., and W. S. Reeburgh (2000), New perspectives on anaerobic methane oxidation, *Environ. Microbiol.*, *2*, 477–484, doi:10.1046/j.1462-2920.2000.00135.x.

Walsh, M. R., S. H. Hancock, S. J. Wilson, S. L. Patil, G. J. Moridis, R. Boswell, T. S. Collett, C. A. Koh, and E. D. Sloan (2009), Preliminary report on the commercial viability of gas production from natural gas hydrates, *Energy Econ.*, *31*, 815–823, doi:10.1016/j.eneco.2009.03.006.

Westbrook, G. K., et al. (Eds.) (1994), *Proceedings of the Ocean Drilling Program*, *Initial Reports*, vol. 146, Ocean Drilling Program, College Station, Tex.

Xu, W., and C. Ruppel (1999), Predicting the occurrence, distribution, and evolution of methane gas hydrate in porous marine sediments, *J. Geophys. Res.*, *104*, 5081–5095, doi:10.1029/1998JB900092.

Yoshioka, H., A. Maruyama, T. Nakamura, Y. Higashi, H. Fuse, S. Sakata, and D. H. Bartlett (2010), Activities and distribution of methanogenic and methane-oxidizing microbes in marine sediments from the Cascadia Margin, *Geobiology*, *8*, 223–233, doi:10.1111/j.1472-4669.2009.00231.x.

Yuan, T., R. D. Hyndman, G. D. Spence, and B. Desmons (1996), Seismic velocity increase and deep-sea gas hydrate concentration above a bottom-simulating reflector on the northern Cascadia continental slope, *J. Geophys. Res.*, *101*, 13,655–13,671, doi:10.1029/96JB00102.